Die approbierte Originalversion dieser Diplom-/Masterarbeit ist in der Hauptbibliothek der Technischen Universität Wien aufgestellt und zugänglich.
http://www.ub.tuwien.ac.at

The approved original version of this diploma or master thesis is available at the main library of the Vienna University of Technology.
http://www.ub.tuwien.ac.at/eng

TECHNISCHE
UNIVERSITÄT
WIEN

Quantum criticality with dynamical mean-field theory

DIPLOMARBEIT

zur Erlangung des akademischen Grades

Diplom-Ingenieur

im Rahmen des Studiums

Technische Physik

eingereicht von

Alexander Vock, BSc
Matrikelnummer 01425054

ausgeführt am Institut für Festkörperphysik

der Fakultät für Physik der Technischen Universität Wien

Betreuung: Associate Prof. Dr. Alessandro Toschi
Mitwirkung: Dr DI Thomas Schäfer

Wien, 10. Mai 2019

Alexander Vock

Alessandro Toschi

Danksagung

For the successful completion of this thesis several persons have played a crucial role. First of all I want to thank my parents and my grandmother for the financial support during the last years. Moreover they created a cultural environment, in which I could build a fundamental basis for my studies. Especially my mother has always encouraged me to improve myself and be opened to new topics, which finally have brought me to the decision of studying physics and to this thesis. I'm really grateful for this!

My supervisor Prof. Alessandro Toschi, to whom I owe great debt of gratitude, brought me, in combination with his really inspiring lectures and his immense knowledge to the world of quantum many body physics. His incomparable support, patience with all my questions, motivation mixed with a refreshing "Italian style" didactic approach are I think unique at the TU Wien and made all the work for this thesis a real enjoyment rather than annoying data analyzation. Caro Alessandro è stato davvero un onore lavorare con te! Moreover he gave me the opportunity for a visit to Paris at the Collège de France, which brings me to next person I'm deeply thankful to: my co-supervisor, Thomas Schäfer. Without his help and support this thesis would not have had this outcome. Despite his immense technical and physical skills, his almost immediate extremly helpful email response (at every hour of the day), Thomas has again showed me how fascinating the work within theoretical solid state physics can be. Thank you very very much for the opportunity to work with you!

I'm also in debt with the colleagues of my working group. Patrick Chalupa, who very patently gave me an introduction to work on the VSC and apart from that he had been helping me very much with insightful discussions till the end of this work. Moreover Severino Adler, Katherina Astleithner have been a great support for the creation of a great office atmosphere and gave me precious input for many problems.

During the past five years many other persons played an important role too. My group of friends, who made my study time an unforgettable experience and a manageable undertaking. With the innumerable discussions we could complete even the most difficult exams, yet not forgetting to enjoy stressless hours. On the other hand, Prof. Ewa Weinmüller, with whom I had the honour to work for 3 years as a tutor, as she gave me the opportunity for a detailed insight into the academic work at a university. Thank you!

I also acknowledge financial support from the Austrian Science Fund (FWF) as the numerical calculations have been performed on the VSC3 cluster.

Kurzfassung

Quantenphasenübergänge (QPÜ) in stark korrelierten Elektronsystemen sind eins der faszinierendsten Phänomene in Festkörperphysik. Die reichhaltigen Phasendiagramme dieser Systeme erlauben die Präsenz von zahlreichen QPÜs. Andererseits existiert noch keine umfassende theoretische Beschreibung der quantenkritischen Eigenschaften korrelierter Elektronen.

Für eines der fundamentalsten Modelle der Festkörperphysik, dem 3D Hubbard Modell, scheint das quantenkritische Verhalten die konventionelle Hertz-Millis-Moriya Theorie zu verletzen. Diese unerwartete Erkenntnis wird der Anwesenheit von speziellen Eigenschaften auf der Fermioberfläche (FO), wie zum Beispiel Kohn Punkte und/oder Linien, zugeschrieben. In diesem Fall sollte die korrekte Beschreibung von 3D korrelierten Metallen bereits durch Dynamische Molekularfeldtheorie (DMFT) erreicht werden. Denn DMFT wahrt die Informationen über die FO Geometrie und behandelt zeitliche Fluktuationen auf korrekte Weise, welche essenziell für Quantenkritikalität sind.

Das Ziel dieser Arbeit ist das Testen der Hypothese, dass eine DMFT Behandlung ausreichend ist, das quantenkritische Verhalten von 3D korrelierten Metallen zu beschreiben ohne auf fortgeschrittene (und wesentlich aufwendigeren!) Quanten Vielteilchen Methoden. Die DMFT Resultate für das 3D Hubbard Modell mit Löcherdotierung haben es uns erlaubt, die Position des quantenkritischen Punkt des magnetischen Übergangs zu bestimmen und die vielversprechenden Trends für die quantenkritischen Exponenten aufzuzeigen.

Abstract

Quantum phase transitions in strongly correlated electron materials are one of the most intriguing phenomena in condensed matter physics. In fact, the rich phase-diagrams of these systems usually allow for the presence of several quantum phase transitions. At the same time, a comprehensive theoretical description of the quantum critical properties of correlated electrons has been not fully developed yet.

For one of the most fundamental model in solid state physics, the 3D Hubbard model, quantum critical behaviour appears to violate the conventional Hertz-Millis-Moriya theory. This unexpected finding has been ascribed to the presence of specific features on the Fermi surface (FS), such as Kohn points and/or lines. In this is the case, the correct description of 3D correlated metal should be already accessible by means of Dynamical Mean Field Theory (DMFT) calculations. DMFT, in fact, preserves the information about the FS geometry and correctly captures temporal fluctuations, crucial for the description of quantum criticality.

The main aim of this work is to test the hypothesis that DMFT treatment is sufficient to describe the quantum critical behaviour of 3D correlated metals, without resorting to more advanced (and much heavier!) quantum many-body schemes. Our DMFT results for the hole-doped 3D-Hubbard model have allowed to determine the location of the quantum-critical point of the magnetic transition and to highlight promising trends for the associated quantum critical exponents.

Contents

Kurzfassung **v**

Abstract **vii**

Contents **ix**

1 Introduction **1**

2 Theory and Methods **5**
- 2.1 Many body physics 5
  - 2.1.1 The one particle Green's function 6
- 2.2 Many body electron correlation modelling 11
  - 2.2.1 Hubbard Model 11
  - 2.2.2 Anderson Impurity Model 13
- 2.3 Dynamical Mean Field Theory 14
  - 2.3.1 Diagrammatic approach of DMFT 15
  - 2.3.2 Self-consistency circle & impurity solver 16
  - 2.3.3 Advantages and limitations of DMFT 21
- 2.4 Two-particle diagrammatics & relevant quantities 22
  - 2.4.1 Response functions 24
  - 2.4.2 Calculation of momentum dependent response functions in DMFT 27

3 Quantum phase transitions **29**
- 3.1 Classical phase transitions and criticality 29
- 3.2 Quantum criticality 32
- 3.3 Theories for phase transitions 34
  - 3.3.1 Landau Theory for classical phase transitions 34
  - 3.3.2 Hertz Millis Moriya Theory for quantum criticality 38
- 3.4 Criticality by means of the Hubbard model 39
  - 3.4.1 Classical criticality for the HM 39

3.4.2 Quantum critical Hubbard model out of half filling 43

4 Phase Diagram and quantum criticality: DMFT results 47

4.1 General determination process for critical exponents 48
4.2 Classical criticality parameter regions 49
4.3 Quantum critical effects 53
4.4 Critical doping n=0.7885? 57

5 Conclusion & Outlook 59

List of Figures 63

Bibliography 67

CHAPTER 1

Introduction

Something deeply hidden had to be behind things.

— Albert Einstein

Look up at the stars and not down at your feet. Try to make sense of what you see, and wonder about what makes the universe exist. Be curious.

— Stephen Hawking

When talking about phase transitions in general, intuitively one can name several every day life phenomena, e.g. the transition from water to ice, as can be easily observed e.g. during a snowfall or when preparing ice cream (and of course in the opposite direction if it is not eaten fast enough and starts melting again). In both cases temperature appears to be the essential parameter that drives this transition. These are so-called 1^{st} order phase transitions, which can be characterized by a jump in the physical properties and the occurrence of metastable phases (e.g. mix of ice and water)

We are mostly interested here to the case of continuous (2^{nd} order) phase transitions[1].Of course, when looking at this problem on a more general perspective one notice that not only temperature driven transitions occur, but there exist several non-thermal parameters, e.g. the magnetic field B, doping n or any other generic parameter g controlling the phase of aggregation of the system of interest.

---

[1] For this class in contrast to the previously described ones no mixed phase occur

There are particularly interesting situation in which, for specific “critical” values of these quantities the temperature of the transition can be brought to zero. Such points in a (g,T) phase diagram are referred as quantum critical points (QCPs). Fig. 1.1 qualitatively illustrates the corresponding situation.

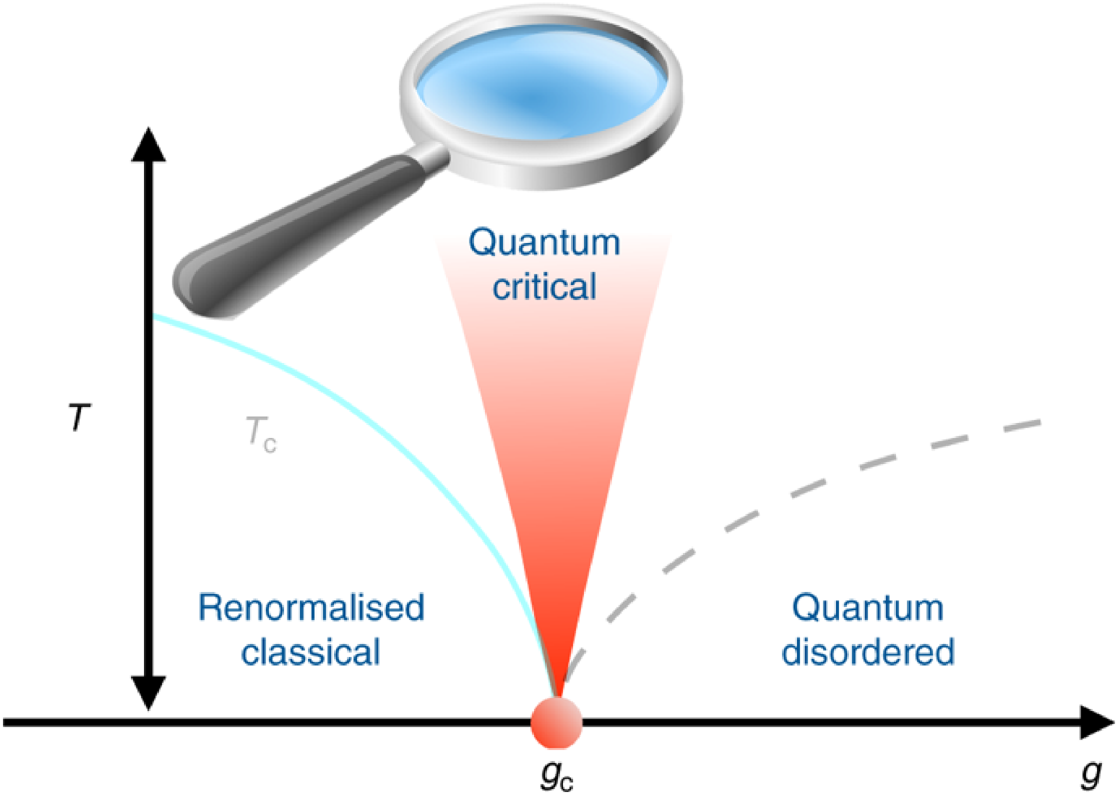

Figure 1.1: This figure, taken from [1], schematically shows the phase transition temperature T_c (light-blue) as a function of a non-thermal parameter g. At a critical value g_c, which defines the QCP, the transition is completely suppressed and $T_c = 0$.

The same picture highlights an important aspect of the quantum phase transition. The problem is not a merely academic $T = 0$ issue, because its occurrence strongly influences the physics of a large, funnel-shaped, parameter regime at finite T. In fact the quantum effects of finite T are often associated with unexpected or exotic phenomena, which explains the great interest among the scientific community. This brings us to another fascinating current field of research, the world of strongly correlated electron systems. These are generally highly sensitive to small changes of external parameters and show a plethora of different physical phases and thus numerous quantum critical points.

From a theoretical point of view there exist several well established standard approaches for describing quantum critical systems, for example the Hertz-Millis-Moriya (HMM) theory [2]. On the other hand, most theoretical models, including (HMM) have significant limitations in applicability as they have been designed for weak-coupling systems, which are often the wrong description for many electron problems, including the model of interest in this work: the 3D Hubbard model.

For theories which describe phase transitions in correlated electron systems, such as DΓA, pioneering attempts have been made to investigate the general quantum critical properties for the 3D Hubbard model [3], which represents the fundamental modelization of strongly correlated electron systems. While no unified theory exists at the moment, it could be shown that in close proximity to the quantum critical point features of the Fermi surface, especially Kohn anomalies, are a crucial ingredient for the functional behaviour of critical exponents and for explaining results that apparently differ from, conventional, e.g. HMM ones.

Interestingly, analytic calculations performed at the RPA level suggest that, the arguably most famous theory of strongly correlated electrons, the dynamical mean-field theory (DFMT) could be already sufficient to fully capture such deviations from the HMM in correlated metals. On the other hand, no closer investigation of the quantum critical region in the 3D Hubbard model have been done hitherto. The lack of previous studies in this rather general framework represents the main motivation for the work done in this thesis. Here systematic calculations of the functional behaviour of the magnetic susceptibility and the correlation length of the 3D Hubbard model have been performed in both classical and quantum criticality parameter regime to test whether, and to what extent, Fermi surface features influences can be properly described within DMFT.

CHAPTER 2

Theory and Methods

Misura ciò che è misurabile, e rendi misurabile ciò che non lo è.

— attributed to Galileo Galilei

In this chapter a compact overview of quantum field theory methods relevant in the context of this thesis is given. After briefly introducing the general expression of the Hamiltonian of an interacting electron system, we will present the formalisms of the one particle Green's function as "pivotal" ingredient for many-electron schemes. Thereafter, we will present some simplified modelizations of the solid state Hamiltonian aiming to capture fundamental many-electron effects of the full problem, such as the Hubbard model and Anderson impurity model (AIM). Furthermore the dynamical mean-field theory (DMFT) will be introduced, as an approach for treating quantum (temporal) fluctuations in a non-perturbative fashion, while totally neglecting spatial ones. For extracting the generalized and the physical susceptibility with DMFT, however, two particle Green's functions computed from the auxiliary AIM are needed. Therefore, at the end of this chapter a brief overview of two particle diagrammatics and quantities is given.

2.1 Many body physics

In solid state physics a quite general expression for a Hamiltonian, including Coulomb interaction between electrons and ions can be written down explicitly by means of the second quantization formalism:

$$\mathcal{H} = \mathcal{H}_0 + V_{ee} \tag{2.1}$$

with

$$\mathcal{H}_0 = \sum_{\sigma=(\uparrow,\downarrow)} \int d^3r \; \Psi^\dagger_\sigma(\vec{r}) \left[-\frac{\hbar^2}{2m}\partial^2 - \sum_l \frac{e^2}{4\pi\epsilon_0} \frac{Z_l}{\left|\vec{r}-\vec{R}_l\right|} \right] \Psi_\sigma(\vec{r})$$

$$V_{ee} = \frac{1}{2} \sum_{\sigma,\sigma'} \int d^3r \; d^3r' \; \Psi^\dagger_{\sigma'}(\vec{r}')\Psi^\dagger_\sigma(\vec{r}) \frac{e^2}{4\pi\epsilon_0} \frac{1}{|\vec{r}-\vec{r}'|} \Psi_{\sigma'}(\vec{r}')\Psi_\sigma(\vec{r})$$

In this notation $\Psi_\sigma(\vec{r})$ and $\Psi^\dagger_\sigma(\vec{r})$ do not represent wave functions but field operators, creating or destroying an electron of charge $-e$ and spin σ at position $\vec{r}$. The index l stands for the lattice ions with their respective charge Z_l and position $\vec{R}$. The quantities m, $\hbar$, ϵ_0 denote the electron mass, Planck constant and dielectric vacuum constant, respectively. The Hamiltonian in Eq. 2.1 is way to complex to be solved exactly in QM, if electron correlations are strong. As we will mention later, approximative models need to be introduced to capture the basic aspects of the many electron problem.

2.1.1 The one particle Green's function

Even by neglecting the motion of the ions (Born-Oppenheimer approximation) the intrinsically many-body effects described by Eq. 2.1 require a quantum field theoretical (QFT) description. In this context the fundamental building block is represented by the one particle propagator, also referred to as one particle Green's function. This quantity is the basic building brick of quantum field theory (QFT). In QFT $\hat{x}(t)$ is no longer an operator but "again" a spatial point associated to an i.e. field operator $\Psi^{(\dagger)}(x,t)$. This (in general time dependent) object creates (or annihilates) a particle in the Fock space of second quantization. Having this argumentation in mind, one also notes that in QFT not the wave function of an electron is the important quantity but the propagation of one electron itself in a "sea" of other electrons. This is reflected in to the definition for the one particle Green function:

$$\begin{aligned} G(\vec{r},t;\vec{r}\,',t') &= -i\langle \mathcal{T}\Psi(\vec{r},t)\Psi^\dagger(\vec{r}\,',t')\rangle = \\ &= -i\left[\theta(t-t')\langle\Psi(\vec{r},t)\Psi^\dagger(\vec{r}\,',t')\rangle - \theta(t'-t)\langle\Psi^\dagger(\vec{r}\,',t')\Psi(\vec{r},t)\rangle\right] \end{aligned} \tag{2.2}$$

Here $\mathcal{T}$ stands for Wick's time ordering operator, guaranteeing always the correct time ordering (i.e. later times on the left) of the operator pair within the expectation value in brackets. This expectation value is with respect to the ground state (for T=0) or thermodynamic ensemble for finite temperatures. As mentioned during the last paragraphs the physical interpretation of this quantity is the propagation of an electron or hole created at $\vec{r}', t'$ and annihilated at $\vec{r}, t$. Alexandre Zagoskin showed in his book *"Quantum Theory of Many-Body Systems"* a quite amusing interpretation of this definition as seen in Fig. 2.1.

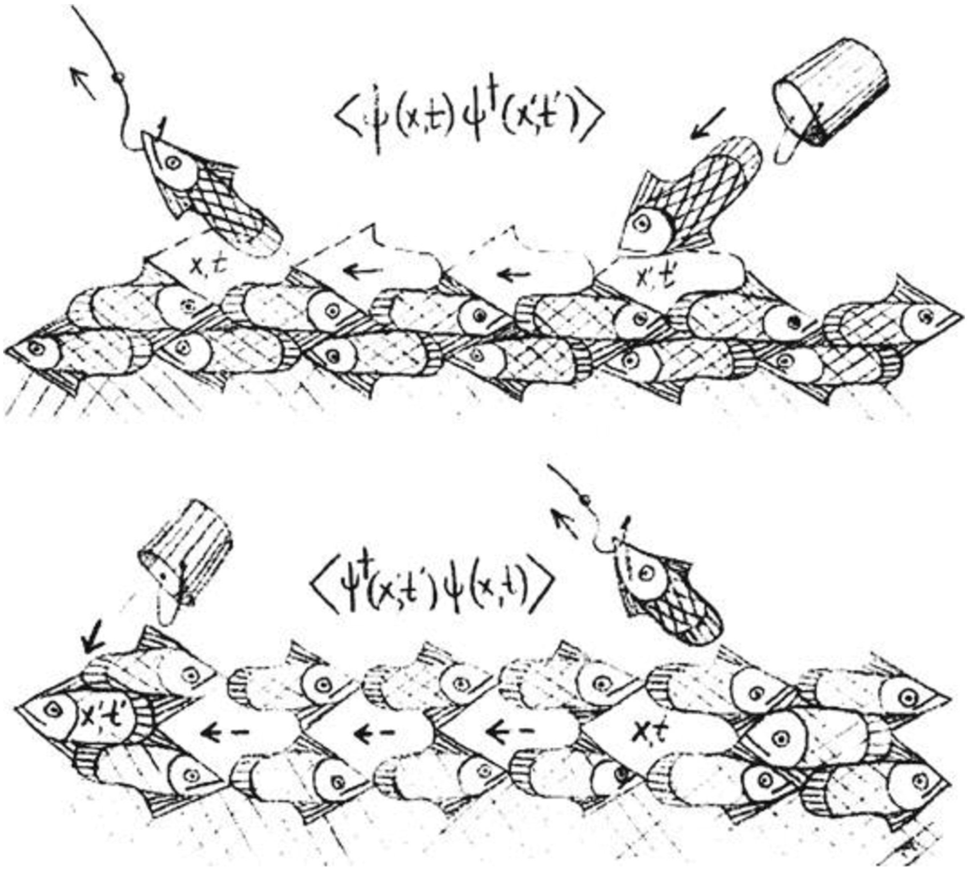
$\langle \psi(x,t)\psi^\dagger(x',t')\rangle$
x,t
x',t'
$\langle \psi^\dagger(x',t')\psi(x,t)\rangle$
x',t'
x,t

Figure 2.1: The illustration is taken from [4] and shows the two possibilities for the electrons in a "fishy" way: either adding (top picture) or removing (bottom picture) an electron at $\vec{x}', t'$ and letting the electron or respectively the hole propagate until $\vec{x}, t$, where it is removed (or added) again

.

In the case of finite temperature calculations, one would obtain time evolution operators with complex time arguments like $e^{i\mathcal{H}(t \pm i\beta)}$, with β representing the inverse temperature $\frac{1}{T}$. To overcome this problem, one performs a so called "Wick rotation"[1] $t \to i\tau$. From now on we will stick to this formalism.

---

[1] named after Gian-Carlo Wick an Italian physicist who originally proposed his theory for a solution in Minkowski space by substituting imaginary-number variables in euclidean space with real ones [5].

If the system is, as in many cases, time and space translational invariant, one can obtain important information by exploiting features of the Fourier transform with respect to the time and space coordinates. For instance, looking at the transform from real space to momentum (k) space translational invariance, which holds for a lattice, leads to [6]:

$$G(\vec{r},\tau;\vec{r}\,',\tau') \Rightarrow G(\vec{r}-\vec{r}\,';\tau,\tau') \overset{\vec{r}\,'\equiv 0}{=} G(\vec{r};\tau,\tau') \tag{2.3}$$

Moreover, for equilibrium system i.e. time independent Hamilton operators also translational invariance in time, which can be proven when Fourier transform $\tau \Rightarrow \omega$ (see [6] for the calculation), simplifies the expression in Eq.(2.2).

$$G(\vec{r};\tau,\tau') \Rightarrow G(\vec{r};\tau-\tau') \overset{\tau'\equiv 0}{=} G(\vec{r},\tau) \tag{2.4}$$

In a second step considering the cyclic properties of the trace and commutation rules for fermionic operators one sees (for details see [6]):

$$G(\vec{r},\tau) = -G(\vec{r},\tau+\beta) \tag{2.5}$$

The periodicity of $G(\vec{r},\tau)$ in the interval $[-\beta,\beta]$ allows to consider discrete Fourier coefficients ω_m ($m \in \mathbb{Z}$). These are for fermions (bosons) the so called Matsubara frequencies, which are the poles of the Fermi-Dirac [Bose-Einstein] distribution function having the form $\omega_m = (2m+1)\frac{\pi}{\beta}$ [$\omega_m = 2m\frac{\pi}{\beta}$] [6]. The Fourier transform of the Green's function then reads as follows:

$$\begin{aligned} G(\vec{r},\tau) &= \frac{1}{\beta}\sum_n G(\vec{r},i\omega_m)e^{-i\omega_m\tau} \\ G(\vec{r},i\omega_m) &= \int_0^\beta G(\vec{r},\tau)e^{i\omega_m\tau} \end{aligned} \tag{2.6}$$

Non interacting Green's function

Now let us explicitly compute the expression for the non interacting Green's function in momentum space, a starting point for several many-body approaches including the more elaborate calculations in DMFT described in section 2.3.

We begin by looking at the Lehmann representation of the Green's function (for a detailed derivation see [6]).

$$G(\vec{k},\tau) = -\frac{1}{Z}\sum_{N,M} e^{-\beta E_N} e^{\tau(E_N - E_M)} \left|\langle N \left| c_{\vec{k}\sigma} \right| M\rangle\right|^2 \tag{2.7}$$

Where Z represents the partition function and $|N\rangle$ as well as $|M\rangle$ are eigenstates of the non interacting Hamiltonian $\mathcal{H}_0$

$$\mathcal{H}_0 = \sum_{\vec{k}\sigma} \epsilon_k \underbrace{c^\dagger_{\vec{k}\sigma} c_{\vec{k}\sigma}}_{\hat{n}_{\vec{k}\sigma}} \tag{2.8}$$

After performing the explicit calculation in the Fock space a simplified expression for $G = G^{(0)}$ can be obtained [6]

$$G^{(0)}(\vec{k},\tau) = -e^{-\epsilon_k\tau}(1 - f(\epsilon_k)) \;{}^{\tau}\overset{\rightarrow}{=}{}^{t}\; G^{(0)}(\vec{k},t) \approx e^{i\epsilon_k t}(1 - f(\epsilon_k)) \tag{2.9}$$

The physical interpretation of this term is transparent. If an electron with respective energy can be added $[1 - f(\epsilon_{\vec{k}}) = 1]$ to the system it will propagate like a plane wave $[\propto e^{i\epsilon_k t}]$. In fact in the non interacting system no scattering events with other electrons take place, leaving the propagation described by $G^{(0)}(\vec{k},\tau)$ undisturbed. The corresponding Fourier transform of Eq.(2.9) reads:

$$G^{(0)}(\vec{k},i\omega) = \int_0^\beta -e^{-\epsilon_k\tau}[1 - f(\epsilon_k)]e^{i\omega_m\tau}d\tau = \frac{1}{i\omega_m - \epsilon_k} \quad . \tag{2.10}$$

Interacting Green's function & Self-Energy

When explicitly taking into account the electronic interaction in the Green's function (denoted $G(\vec{k},i\omega_m)$), a new quantity namely the self-energy $\Sigma(k,i\omega_m)$ can be introduced. Thus is defined as a physical difference of the two cases and for the sake of simplicity the "free" non-interacting Green function will be defined as $G^{(0)}(\vec{k},i\omega) \equiv G_0(\vec{k},i\omega)$.

$$\Sigma(\vec{k},i\omega_m) = G_0^{-1}(\vec{k},i\omega) - G^{-1}(\vec{k},i\omega), \tag{2.11}$$

This equation, referred in the literature as the Dyson equation, can be solved for G and by inserting the expression from Eq. 2.10 one obtains:

$$G(\vec{k}, i\omega) = \frac{1}{i\omega_m - \epsilon_k - \Sigma(\vec{k}, i\omega_m)} \tag{2.12}$$

When dealing with the Dyson equation, one encounters the concept of one particle reducibility. This could be understood as cutting an internal Green's function line which separates the diagram into two independent ones. Figure 2.2 illustrates this idea by means of the Dyson equation.

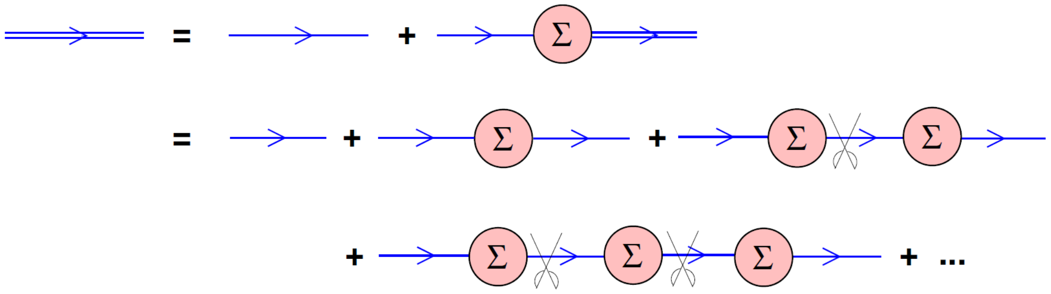

Figure 2.2: When expanding the interacting Green function in the Dyson equation a resulting infinite sum of 1P reducible diagrams appears. These corresponding classification can be done by an imaginary pair of scissors showing that through cutting an internal Green function line two separate Feynman diagrams can be obtained [7].

To better understand the physical meaning of the self-energy, let us consider the case of Fermi liquid theory, which renormalizes non-interacting quantities for a qualitative understanding. Such renormalization can be understood microscopically by expanding $\Sigma(k, i\omega_m) = \mathrm{Re}\,\Sigma(k, i\omega_m) + \mathrm{Im}\,\Sigma(k, i\omega_m)$ up to 1^{st} order around the Fermi energy level ($E \approx E_f$, $k \rightarrow k_F$, $i\omega_m \rightarrow 0$) and inserting it into Eq. 2.12. Consequently, the Fourier transform of the result (for details see [6]) reads:

$$G(t) \approx e^{-i(\epsilon_k + \mathrm{Re}\,\Sigma(k_F))t} e^{-\gamma t}, \quad \gamma = -\,\mathrm{Im}\,\Sigma(k_F) \tag{2.13}$$

Now it can be easily seen that the real part of $\Sigma(k)$ leads to corrections of the non-interacting dispersion or chemical potential, whereas the imaginary part depicts the (now) finite lifetime of the one particle-excitations: the so-called Landau quasi-particles. Finally, it should be mentioned at this point that the Green's function and even more the self-energy, despite of their importance still remain rather abstract concepts from the experimental point of view. In order to relate them to measurable quantities one usually looks at the spectral function which is accessible through, e.g. Angle Resolved Photoemission Spectroscopy (ARPES). For a detailed discussion of the topic see [8].

2.2 Many body electron correlation modelling

As the Hamiltonian in Eq. 2.1 cannot be solved exactly, simplified model expressions have been introduced. For strongly correlated orbitals a typical approach consists in treating only the major part of the interactions meaning only its local part. These approximations lead to significantly simpler Hamiltonians, which yet often capture the fundamental properties of electronic correlations. In the next paragraphs the arguably two most fundamental models for many body systems, the Hubbard model and the Anderson Impurity model, will be briefly introduced.

2.2.1 Hubbard Model

The Hubbard model has been originally proposed in the 1960s to describe electrons in 3d transition metals [9]. Since the radial wave function of the 3d electrons, as well as that for 4f electrons, has a small spatial extent, this usually leads to an effectively strong electronic interaction. The quintessence of the independently proposed "Ansatz" by Hubbard [9], Gutzwiller [10] and Kanamori [11] was to assume a purely local, strongly screened interaction (U) leading, for a single orbital case (which is the one we consider in this work), to a Hamiltonian of the form:

$$\mathcal{H} = -t \sum_{(i,j),\sigma} c^{\dagger}_{i\sigma} c_{j\sigma} + U \sum_{i=1}^{N} n_{i\uparrow} n_{i\downarrow}, \tag{2.14}$$

where the first part of the Hamiltonian describes the transit of the electrons from site i to j and the second part the energy cost for double occupations at one site.

But let's go back one step and give a mathematically accurate deviation for Eq. 2.14.

Starting from the expression given by Eq. 2.1 one tries to simplify the $\mathcal{H}_0$ term by a superposition of atomic orbital states called Wannier states. An important feature of these states is the fact, that they form an orthonormal basis of the single particle Hilbert space. The basis is defined by unitary transformation between real ($\vec{r}$) and Wannier space (whose states are typically labeled):

$$\Psi^{\dagger}_{\sigma}(\vec{r}) = \sum_{i=1}^{N} \psi^{*}_{\vec{R}_i}(\vec{r}) c^{\dagger}_{i\sigma}. \tag{2.15}$$

By Fourier transforming the Wannier operators $c^\dagger_{i\sigma}$ to momentum space one can also rewrite the expression for H_0 in momentum space (for the mathematical details see [12]):

$$\mathcal{H}_0 = \sum_{\vec{k}} \epsilon_k c^\dagger_{k\sigma} c_{k\sigma} = \sum_{ii'} t_{ii'} c^\dagger_{i\sigma} c_{i'\sigma} \tag{2.16}$$

where $t_{ii'}$ stands for

$$t_{ii'} = \frac{1}{N} \sum_{\vec{k}} e^{i\vec{k}(\vec{R}_i - \vec{R}_{i'})} \epsilon_k = \int d^d r \; \psi^*_{\vec{R}_i} \frac{\hbar^2 \partial^2}{2m} \psi_{\vec{R}'_i}.$$

When applying a similar procedure to the interaction term in 2.1 one obtains:

$$\mathcal{H} = \sum_{i,i'} t_{ii'} c^\dagger_{i\sigma} c_{i'\sigma} + \sum_{ii'jj'} U_{ii'jj'} c^\dagger_{i\sigma} c^\dagger_{i'\sigma} c_{j\sigma} c_{j'\sigma}. \tag{2.17}$$

In the case of weak orbital overlaps only the on-site Coulomb interaction gives a significant contribution. If one assumes also only nearest neighbour uniform hopping we finally obtain the expression of Eq. 2.14 for the single band case. The $c^\dagger_{i\sigma}$ and $c_{i\sigma}$ are creation and annihilation operators for electrons and $n_{i\uparrow}, n_{i\downarrow}$ give the number of spin-up/spin-down electrons at a lattice site i. It now becomes evident that the second term describes the of potential energy of the problem, since the energy U has to be paid only in case of double occupancy, whereas the first term is the kinetic energy. Figure 2.3 shows a schematic illustration of the main features depicted by the Hubbard Model.

It should be mentioned that although the Hubbard Hamiltonian has a quite simple form, only few cases (i.e. 1d and $d = \infty$) are exactly solvable today. This is due to the competition of kinetic and potential terms in Eq. 2.14: the first is diagonal in momentum (Bloch) space and the second in real (actually Wannier) space, which makes a non-perturbative solution of the problem very difficult. On the other hand, due to its fundamental nature the Hubbard model is often a standard starting point for solid state correlation investigation. With the help of dynamical mean field theory, described in section 2.3, and its cluster [13] diagrammatic extensions (e.g. DGA [14]) one has an adequate tool to treat the Hubbard Model satisfactorily, as it is done in the work of this thesis.

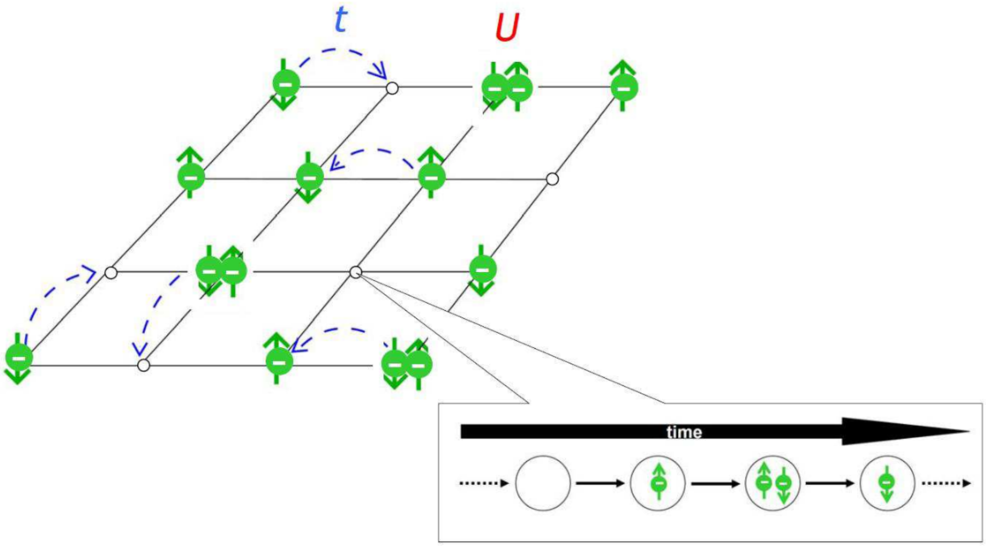

Figure 2.3: The illustration taken from [15] shows the electronic microscopic processes of the Hubbard model: Hopping from site i to j and ii whenever two electrons with opposite spin are on the same lattice site, the local Coulomb interaction U must be paid.

2.2.2 Anderson Impurity Model

Approximately thirty years after the experimental discovery that small amounts of ion magnetic impurities may cause a pronounced minimum in the electric resistivity, by de Haas, de Boer, and van den Berg in 1934 [16], Kondo firstly described this phenomenon accurately [17]. A big step forward towards the microscopic understanding of this problem came from Philip Warren Anderson who suggested a Hamiltonian which models the interaction of itinerant band electrons states with a simplified localised magnetic moment of the ion impurity [18]. This expression has the following form in second quantization:

$$\mathcal{H}_{AIM} = \sum_{k\sigma} \epsilon_k a^\dagger_{k\sigma} a_{k\sigma} + \sum_{k\sigma} V_k (c^\dagger_\sigma a_{k\sigma} + a^\dagger_{k\sigma} c_\sigma) + U n_\uparrow n_\downarrow - \mu(n_\uparrow + n_\downarrow) \tag{2.18}$$

The $a^\dagger_{k\sigma}, a_{k\sigma}$ stand for creation and annihilation operators for an electron with spin σ at an energy bath ϵ_k, whereas $c^\dagger_\sigma, c_\sigma$ create/destroy an electron with its respective spin at the impurity site. The quantity V_k is a measure for the hybridization strenght between the impurity and the electron bath. U is again the Coulomb repulsion for double occupancy at the impurity site, where $n_{\uparrow,\downarrow}$ is a number operator for electrons there. By construction the Anderson Impurity model appears thus also suited for treating the local (on-site) electronic correlations especially in the Hubbard model system.

2.3 Dynamical Mean Field Theory

When looking at the Hubbard model in Eq. 2.14 “conventional” Hartree-Fock type theories, which are based on factorizing correlation functions, are not able to properly capture the most interesting regime of strong electronic correlation. Therefore controlled not approximative techniques are required. Most of them start from a perturbative treating of the problem. Either the interaction term U is very small, or the hopping term t. But what happens in case of intermediate coupling $U/t \approx 1$? Actually DMFT can also be formulated as a theory in the limit of a large parameter, the coordination number z. Yet, no other restrictions are made and local dynamics of the system is, thus, retained. Furthermore 3D systems, which are evidently quite relevant for physicists, already have a large z[2], i.e. for fcc z=12. Now what is the quintessence of DMFT?

> *“DMFT maps a many electron problem onto a single site one, which has to be determined self-consistently. Hence DMFT can be understood as non-perturbative approximation scheme for the investigation of models and materials with correlated electrons in $d \leq \infty$"*

The last sentence has been formulated by Dieter Vollhardt [19], who together with Walter Metzner, Antoine Georges and Gabriel Kotliar has been one of the pioneers of DMFT.

Before discussing DMFT in more detail, let us have a brief look at the general construction scheme for “classic” mean field theories by discussing the famous Ising model.

Also in this case, by taking the limit $z \to \infty$ the spin-spin interaction is replaced by a mean field term [20], describing the interaction of a single spin with a field (often referred as mean (molecular) field). Of course when considering $z \to \infty$, the coupling constant J has to be rescaled thus guaranteeing a finite expression for the mean-field term:

---

[2] It should be mentioned here that for theorists in this sector 12 is already quite near to ∞. One might think this is a joke, but experimental results confirm this assumption in this research field.

$$H_{Ising} = -\frac{1}{2}\, J \sum_{\langle R_i, R_j \rangle} S_i S_j \Longrightarrow H_{MF} = -h_{MF} \sum_{R_i} S_i$$

$$\text{with } h_{MF} = J \sum_{R_j}^{(i)} S_j \quad \text{and } J \rightarrow \frac{J^*}{Z}, \quad J^* = const \tag{2.19}$$

2.3.1 Diagrammatic approach of DMFT

In the quantum regime one can apply some procedure to the Hubbard Hamiltonian. In this case, a proper rescaling of the kinetic energy term must be considered, while the potential or interaction term is completely local and therefore is dimension independent. Following the idea of Metzner and Vollhardt [21], we can exploit the following result that due to the central limit theorem resulting Gaussian DOS remains finite for $d \to \infty$ only if:

$$t \longrightarrow \frac{t^*}{\sqrt{d}} \quad t^* = const. \tag{2.20}$$

The following derivation is taken from [21], where the most important steps are summarized now.

- Looking at kinetic energy for T=0 and U=0 we obtain

  $$E_{kin} = -t \sum_{\langle \vec{R}_i \vec{R}_j \rangle} \sum_{\sigma} g^0_{ij,\sigma}, \quad g^0_{ij,\sigma} = \langle c^\dagger_{i\sigma} c_{j\sigma} \rangle. \tag{2.21}$$

  Where the quantity $g^0_{ij,\sigma}$ can be seen an amplitude for hopping processes between $\vec{R}_i$ and $\vec{R}_j$. Thus the probability, which is proportional to its square, behaves like $1/d$.

- In the limit $d \to \infty$ one gets:

  $$g^0_{ij,\sigma} \sim \mathcal{O}\left(\frac{1}{\sqrt{d}}\right) \tag{2.22}$$

- The non-interacting Green's function 2.2 obeys the identical scaling relation

- Moreover, the Green's function and its Fourier transform have to follow the scaling, since it is not time dependent, for all times.

- Even for $d \to \infty$ particles remain mobile and may hop to d nearest neighbours.

- This leads to:
$$G^0 \sim \mathcal{O}\left(1/d^{||\vec{R}_i - \vec{R}_j||/2}\right) \tag{2.23}$$
where the quantity $||\vec{R}|| = \sum_d^{n=1} \vec{R}_n$ is denoted in the "New York metric" allowing only hopping on horizontal or vertical lines.

- This property leads to a collapse of all connected, irreducible perturbation theory diagrams in position space.

The most important insight of this derivation is the fact that Metzner and Vollhardt could demonstrate that the self-energy skeleton diagrams become purely local [21]. This means that their Fourier transform will be momentum independent.

$$\Sigma_\sigma(\vec{k}, \omega) \equiv \Sigma(\omega) \quad \text{for} \quad d \to \infty \tag{2.24}$$

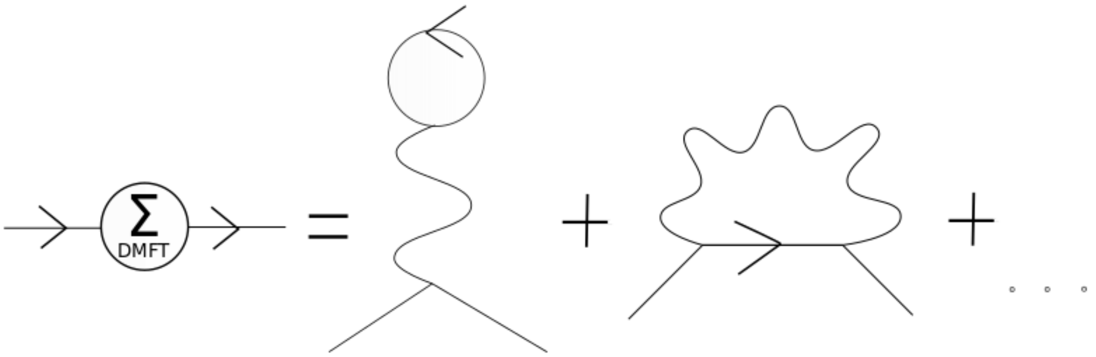

Figure 2.4: This illustration shows Self Energy expressed as the sum of all one particle irreducible diagrams.

Diagrammatically, DMFT corresponds, thus, to consider all completely local one-particle irreducible diagrams[3] for the electronic self-energy, shown in Fig. 2.4. In a physical context this means considering only the local part of the electronic correlation but in a fully non perturbative way.

2.3.2 Self-consistency circle & impurity solver

From the algorithmic point of view, the crucial step when performing DMFT calculations is the solution of the local problem, where $G_{loc}(\omega)$, the local Green function, as well as the local self-energy $\Sigma(\omega)$ represent local observables, related to a dynamical, in this context frequency dependent, mean field $h_{eff}(\omega)$. Now as *A. Georges et al* [13] have summarized in their 1996 review (having achieved the status of "Encyclopaedia" for DMFT by now) by mapping the problem to the Anderson impurity model, the same diagrams for the DMFT self-energy can be obtained. If the impurity interaction coincides with the original Hubbard model one and the electron bath is properly chosen. Additionally this approach links DMFT to AIM, for which elaborate numerical codes have already been developed during the 1980's. In Fig. 2.5 the hybridization between bath and impurity electron is schematically shown.

---

[3] 1P irreducible diagrams are the ones which cannot be separated in two by cutting one internal fermionic line.

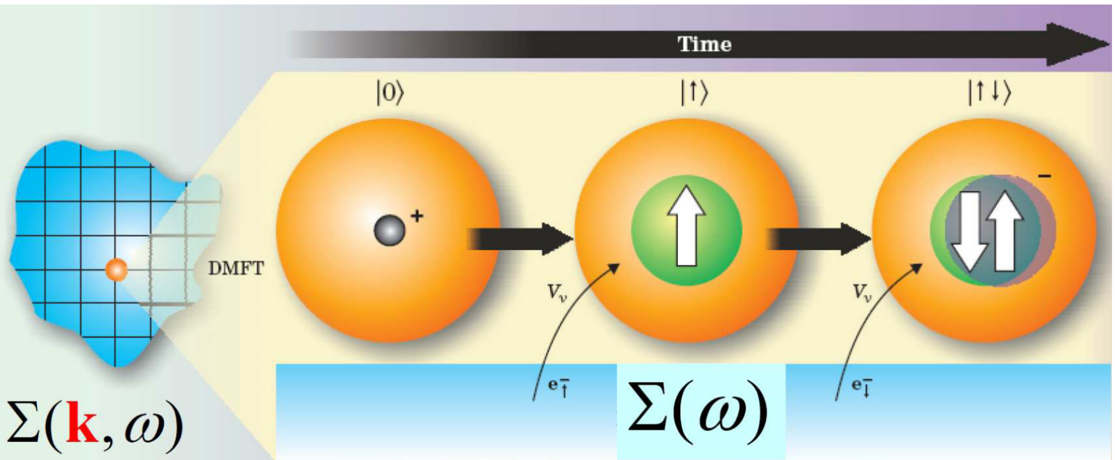

Figure 2.5: This figure, which is taken from [15], illustrates that DMFT is essentially a mapping of the d-Dimensional Hubbard Model and its corresponding self-energy $\Sigma(k,\omega)$ onto a single site (described by its determined, auxiliary AIM). Thus the impurity and the bath electrons hybridize resulting in a local problem, where the self-energy is momentum independent.

It is now crucial to impose a condition that links the, sort of properly chosen auxiliary AIM to the DMFT problem by setting $G_{loc}(\omega) = G_{AIM}(\omega)$. This prerequisite serves as self-consistency condition in an iterative DMFT loop. The relation of this two quantities is associated with the local self-energy $\Sigma(\omega)$ which on the one hand is included in the AIM Dyson equation:

$$\mathcal{G}_0^{-1}(\omega) = G_{AIM}^{-1}(\omega) + \Sigma(\omega) \tag{2.25}$$

and on the other hand defines the local Green's function too:

$$G_{loc}(\omega) = \sum_{k \in BZ} \frac{1}{\omega - \epsilon_k - \Sigma(\omega)} \tag{2.26}$$

The quantity $\mathcal{G}_0^{-1}(\omega)$ is describing the hybridization with the electronic bath of the auxiliary AIM and acts like the Weiss mean field in this quantum case.

In Fig. 2.6 a full DMFT self-consistency loop circle is shown. The most time-consuming part from the numerical point of view is doubtlessly finding a solution of the impurity problem. Currently there exist several different impurity solvers, whereby quantum Monte Carlo (QMC), which will be briefly presented in the following section and exact diagonalization (ED) are the most common ones.

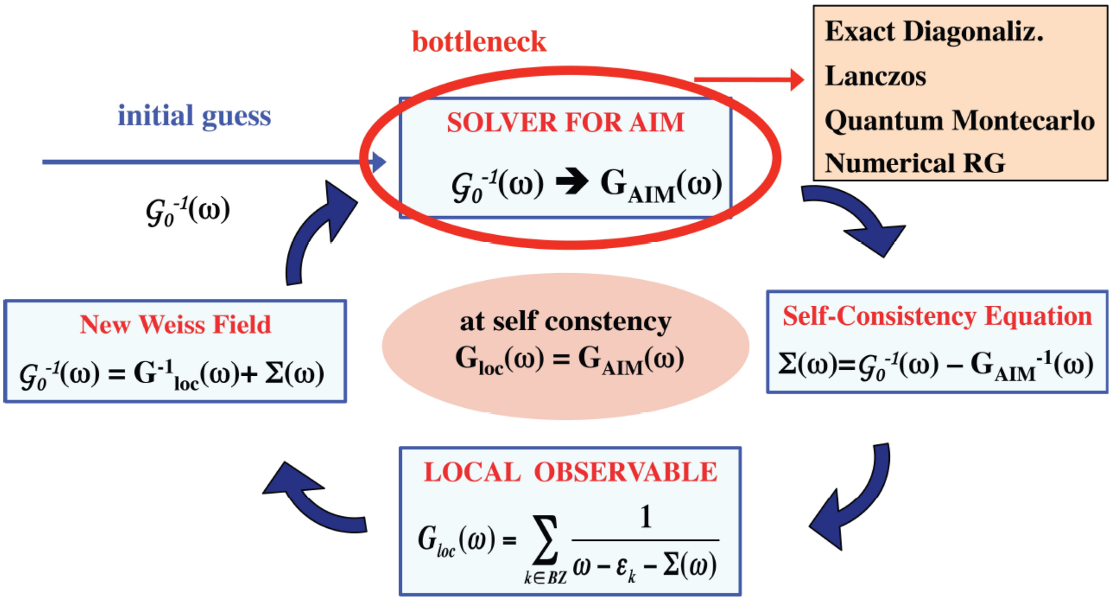
bottleneck
initial guess
$\mathcal{G}_0^{-1}(\omega)$
SOLVER FOR AIM
$\mathcal{G}_0^{-1}(\omega) \rightarrow G_{AIM}(\omega)$
Exact Diagonaliz.
Lanczos
Quantum Montecarlo
Numerical RG
New Weiss Field
$\mathcal{G}_0^{-1}(\omega) = G^{-1}_{loc}(\omega) + \Sigma(\omega)$
at self constency
$G_{loc}(\omega) = G_{AIM}(\omega)$
Self-Consistency Equation
$\Sigma(\omega) = \mathcal{G}_0^{-1}(\omega) - G_{AIM}^{-1}(\omega)$
LOCAL OBSERVABLE
$G_{loc}(\omega) = \sum_{k \in BZ} \frac{1}{\omega - \varepsilon_k - \Sigma(\omega)}$

Figure 2.6: This figure [22] summarizes the process for performing a DMFT self consistency loop. As highlighted in the picture the most challenging step is the numerical solution of the AIM.

Impurity solver

Since for the work done in this thesis exclusively QMC algorithms will be utilised, this method be described in a brief manner now. One of the most popular QMC schemes was the Hirsch-Fye (HF) method [23], formulated for the first time about 30 years ago. Here the interaction Anderson impurity model is mapped onto a sum of non-interacting problems with a single impurity particle influenced by an field with explicit time dependence. Consequently this sum is calculated by standard

Monte Carlo sampling. Even if for calculations performed in this work CT-QMC method will be used, during the next paragraphs first the most important steps of HF-QMC for a basic QMC understanding will be presented, which can be found in a more detailed manner in [13]:

- First one separates the Anderson Hamiltonian for a local impurity $\mathcal{H}$ into an non-interaction part $\mathcal{H}_0$ and an interacting one $\mathcal{H}_1$.
- In this numerical step the time interval $[0, \beta]$ is discretised into L step, often referred as Trotter discretization:

$$\Delta\tau = \frac{\beta}{L}. \tag{2.27}$$

- Having performed this step, the partition function can be written considering the time slices and additionally when applying the Trotter-Suzuki decomposition a decomposed term, with respect to interacting part of $\mathcal{H}$, can be achieved, with an error $\mathcal{O}(\Delta\tau^2)$.

$$Z = \mathrm{Tr}\left(e^{-\beta\mathcal{H}}\right) = \mathrm{Tr}\left(\prod_{i=1}^{L} e^{-\Delta\tau\mathcal{H}}\right) \tag{2.28}$$

$$e^{-\Delta\tau\mathcal{H}} = e^{-\frac{\Delta\tau\mathcal{H}_0}{2}} e^{-\Delta\tau\mathcal{H}_1} e^{-\frac{\Delta\tau\mathcal{H}_0}{2}} + \mathcal{O}(\Delta\tau^2) \tag{2.29}$$

$$Z \approx \mathrm{Tr}\left(\prod_{i=1}^{L} e^{-\Delta\tau\mathcal{H}_0} e^{-\Delta\tau\mathcal{H}_1}\right) \tag{2.30}$$

- By utilising an auxiliary field, the Hubbard-Stratonovich, and exploiting Hirsch's identity Eq. 2.31 designed for local interaction Hamilton operators, the interacting problem has been mapped onto the sum over all possible configurations of the auxiliary field of non-interacting Ising-spins.

$$e^{-\Delta\tau U\left(n_{i\uparrow}n_{i\downarrow} - \frac{1}{2}\left(n_{i\uparrow}+n_{i\downarrow}\right)\right)} = \frac{1}{2}\sum_{s_i=\pm1} e^{\lambda s_i\left(n_{i\uparrow}-n_{i\downarrow}\right)} \tag{2.31}$$

$$\lambda = \arccos\left(e^{\frac{\Delta\tau U}{2}}\right) \tag{2.32}$$

- The partition function has now the following form

$$Z = \sum_{s_1,\dots,s_L} \det\left[G_\uparrow^{-1}(s_1, \dots, s_L)\right] \det\left[G_\downarrow^{-1}(s_1, \dots, s_L)\right] \tag{2.33}$$

- The expression inside the sum of Eq.(2.33) represent the stochastic weight of the Monte Carlo sampling. Moreover the single spin flip Markov chain outcome is represented by the $s_1, ..., s_L$ configurations.

However even if HF-QMC has been state of the art up to the late 2000's, it presents limitations especially when treating low-temperature regions in the phase diagram. As the equal spaced time steps are proportional to $\beta = \frac{1}{T}$ and theory as a whole is conceived for local (small) interactions. In the case of large U and low temperatures systematic errors become significant and should be treated carefully.

To overcome some of these difficulties, nowadays continuous time QMC (CT-QMC), has become the new standard technique, which will be also utilized for this work. Here again, the starting point is the separation of the Hamiltonian $\mathcal{H}$ into a $\mathcal{H}_a$, containing the bath- and local Hamiltonian (which is the following expression in interaction representation $\mathcal{H}_{loc} = \mathcal{H}^0_{loc} + \mathcal{H}^I_{loc}$) and $\mathcal{H}_b$ term, though this time the partition function $Z =^{-\beta\mathcal{H}}$ is written in the interaction representation with respect to $\mathcal{H}_a$ and expanded in powers of $\mathcal{H}_b$ [24]:

$$Z = Tr\left[T_r e^{-\beta\mathcal{H}_b} exp\left[-\int_0^\beta d\tau \mathcal{H}_b(\tau)\right]\right]$$

$$= \sum_k (-1)^k \int_0^\beta d\tau_1 \cdots \int_{\tau_{k-1}}^\beta Tr\left[e^{-\beta\mathcal{H}_b}\mathcal{H}_b(\tau_k)\mathcal{H}_b(\tau_{k-1})\cdots\mathcal{H}_b(\tau_1)\right] \tag{2.34}$$

The big advantage of this approach is the fact of starting directly in continuous time and thus avoiding discretisation errors. With respect to coupling strength two different algorithm will be briefly sketched now, for a detailed review on CT-QMC one can refer to [24] of which the following explanations have been taken from. For weak-coupling systems the interaction expansion algorithm (CT-INT) is used [25]. Having as starting point Eq. 2.34 $\mathcal{H}_b$ is assumed as interaction part of the local Hamiltonian and $\mathcal{H}_b$ thus is $\mathcal{H}_a = \mathcal{H}_{bath} + \mathcal{H}_{hyb} + \mathcal{H}^0_{loc}$. More important for the work in this thesis is the so called hybridization expansion (CT-HYB) [26]. This algorithm is used in *w2dynamics* code [27], which has been utilized in this work. In contrast to CT-INT at CT-HYB $\mathcal{H}_b$ is assumed as hybridization term $\mathcal{H}_{hyb}$ and thus $\mathcal{H}_a = \mathcal{H}_{bath} + \mathcal{H}_{loc}$. This technique has several advantages, e.g. the expansion order is much smaller than for CT-INT in case of strong coupled systems. This means lower temperatures are more accessible, for a detailed discussion see [28].

2.3.3 Advantages and limitations of DMFT

Surely one of the main advantages DMFT gives is the non-perturbative description of the Mott insulator transition (MIT), where the spectral function of a metal can subsequently turn to an insulator if the local Coulomb interaction U is large enough. Before DMFT no globally valid[4] theory existed. For instance density functional theory (DFT) is restricted to quasi-particles regions, if U remains small, whereas the atomic limit is an adequate tool for Hubbard model description only in the very large U limit. DMFT though, could be seen as a theory that fully captures the MIT as gradually spectral weight transfer from quasi particle peaks to Hubbard sub-bands of the correlated metallic state [29].

An important feature of DMFT, as mentioned before, is momentum independence of the self-energy $\Sigma(\omega)$. Due to this circumstance the Fermi surface geometry is not changed by interactions[5]. This holds also for the spectral function and the Fermi energy, which is only shifted uniformly[15].

On the other hand, a drawback of DMFT is the fact that even if temporal or quantum fluctuations are described accurately, spatial ones are not treated at all, since DMFT remains mean field level from the spatial point of view. This proves to be a poor description for regions near second-order phase-transitions (here the correlation length ξ goes to ∞). The same considerations apply to the cases of low dimension (1D or 2D)[6] as DMFT becomes exact only for $d = \infty$.

We recall that when applying DMFT to systems with finite dimensions, the self-consistency is valid only for one particle quantities. As a consequence of this, the (local) susceptibility (a two particle density correlation function) of the DMFT isn't corresponding to the same quantity of the AIM anymore. These considerations are of particular importance for approaches which go beyond the limitations of DMFT.

Another important reason for having a more detailed look at two particle quantities is their importance when performing the Bethe-Salpeter Equation for the extraction of response functions in DMFT. Hence, a brief introduction to two particle quantities and extractions of these will be given in the next section , which has been adapted from [30].

---

[4] In this context “globally” intends different regions of the phase diagram

[5] It should be mentioned here, that of course the notion of a Fermi surface in $d = \infty$ might appear a little complicated, as the dispersion function is not smooth at all.[15]

[6] 3D is still close enough to obtain satisfying results with DMFT

2.4 Two-particle diagrammatics & relevant quantities

In order to calculate the main quantity of interest in this thesis, i.e. the magnetic susceptibility within DMFT, one has to move to the two-particle level of the diagrammatics. The two particle Green function is introduced as follows:

$$G_{2,\sigma_1,\ldots\sigma_4} = \langle \mathcal{T} c^\dagger_{\sigma_1}(\tau_1) c_{\sigma_2}(\tau_2) c^\dagger_{\sigma_3}(\tau_3) c^\dagger_{\sigma_4}(\tau_4) \rangle \tag{2.35}$$

This immediately leads to the definition for a generalized susceptibility, which is usually used in the two particle case [31]. Analogously to the 1P case, due to periodicity, the time interval $[0, \beta]$ is sufficient and $\tau_4 = 0$ can be chosen since time-translational invariance in the Hamilton operator holds.

$$\chi_{\sigma_1,\sigma_2,\sigma_3,\sigma_4} = G_{2;\sigma_1,\sigma_2,\sigma_3,\sigma_4}(\tau_1,\tau_2,\tau_3,0) - G_{1;\sigma_1,\sigma_2}(\tau_1,\tau_2) G_{1;\sigma_3,\sigma_4}(\tau_3,0) \tag{2.36}$$

When Fourier transforming the above quantity, 2 conventions exist the particle-hole (ph) and particle-particle (pp) notation, which are shown in Eq. 2.37 and in Fig. 2.7. As for the spin coordinates, often linear combinations are build for a more physical description for example the spin channel one: $\chi_s = \chi_{ph,\uparrow\uparrow} - \chi_{ph,\uparrow\downarrow}$.

$$\begin{aligned} \chi^{\nu,\nu',\omega}_{ph;\sigma,\sigma'} &= \int_0^\beta d\tau_1 \tau_2 \tau_3 \chi_{\sigma,\sigma'}(\tau_1,\tau_2,\tau_3) e^{-i\nu\tau_1} e^{i(\nu+\omega)\tau_2} e^{-i(\nu'+\omega)\tau_3} \\ \chi^{\nu,\nu',\omega}_{pp;\sigma,\sigma'} &= \int_0^\beta d\tau_1 \tau_2 \tau_3 \chi_{\sigma,\sigma'}(\tau_1,\tau_2,\tau_3) e^{-i\nu\tau_1} e^{i(\omega-\nu')\tau_2} e^{-i(\omega-\nu)\tau_3} \end{aligned} \tag{2.37}$$

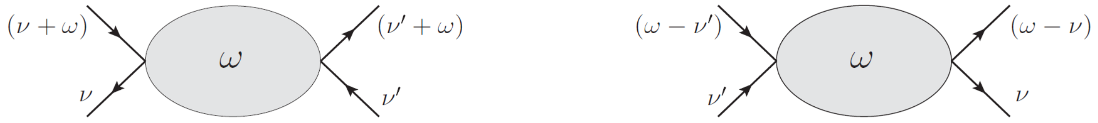

Figure 2.7: This figure, which has been taken from [31] show a particle-hole scattering event on the left side and a particle-particle one on the right

Hitherto we have encountered expressions for the so called generalized susceptibility. However, this quantity is not easily experimentally accessible and the physical susceptibility of the system instead is obtained by summing over both fermionic Matsubara frequencies:

$$\chi_s(\omega) = \frac{1}{\beta^2}\sum_{\nu\nu'} \chi_s^{\nu\nu'\omega} \tag{2.38}$$

From now on, however, we will stick to $\chi_{ph} \equiv \chi$, as this quantity is utilized for this work. The generalised susceptibility can be diagrammatically divided into a “bare” propagation term and an interaction term the so-called vertex corrections:

$$\chi_{\sigma,\sigma'}^{\nu,\nu',\omega} = \chi_0^{\nu,\nu',\omega}\delta_{\sigma,\sigma'} - G_\sigma(\nu)G_\sigma(\nu+\omega)F_{\sigma,\sigma'}^{\nu,\nu',\omega}G_\sigma(\nu')G_\sigma(\nu'+\omega) \tag{2.39}$$

where the first term on the right side looks as follows

$$\chi_0^{\nu,\nu',\omega} = -\beta G_\sigma(\nu)G_\sigma(\nu+\omega)\delta_{\nu\nu'} \tag{2.40}$$

Figure 2.8 shows the form of 2.39 from a diagrammatic point of view.

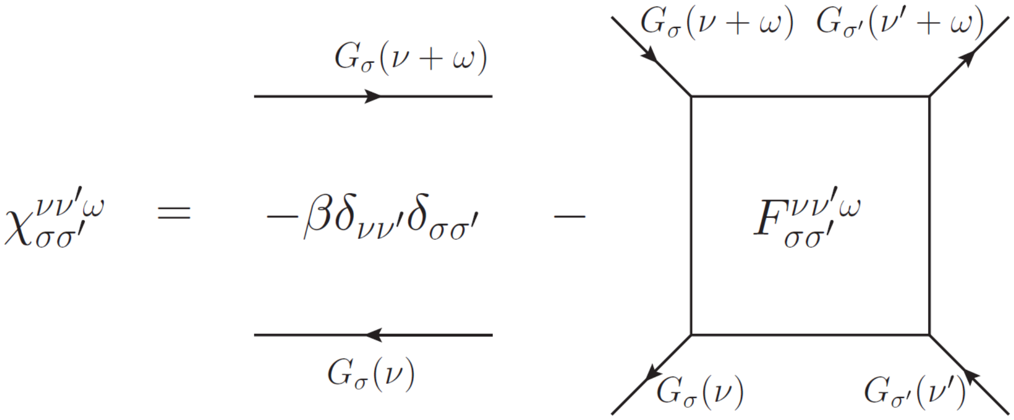
$\chi_{\sigma\sigma'}^{\nu\nu'\omega}$
=
$G_\sigma(\nu+\omega)$
$-\beta\delta_{\nu\nu'}\delta_{\sigma\sigma'}$
$G_\sigma(\nu)$
−
$G_\sigma(\nu+\omega)$
$G_{\sigma'}(\nu'+\omega)$
$F_{\sigma\sigma'}^{\nu\nu'\omega}$
$G_\sigma(\nu)$
$G_{\sigma'}(\nu')$

Figure 2.8: This figure, which has been again taken from [31] shows the diagram corresponding to the independent propagation of two particles as well as that describing the scattering events. The sum of the two contributions yields the generalized susceptibility $\chi_{\sigma,\sigma'}^{\nu,\nu',\omega}$

In this context F denotes the full vertex function which is made up of all two-particle connected diagrams. In turn this, physically interpreted, scattering term can be further decomposed due to reducibility at the 2P level: a diagram is called 2P reducible, of one can cut two fermionic lines, and by this, the diagram will split into two. For this situation not only one way exists to cut a diagram but 3, the particle-particle channel (pp), the transversal particle-hole (ph) and the longitudinal particle-hole one ($\overline{ph}$). This immediately leads to another decomposition for the complete vertex function F into a fully irreducible part Λ and reducible parts Φ_r for the specific channels $r = (pp, ph, \overline{ph})$. The resulting equation is called the parquet equation.

$$F = \Lambda + \Phi_{pp} + \Phi_{ph} + \Phi_{\overline{ph}} \tag{2.41}$$

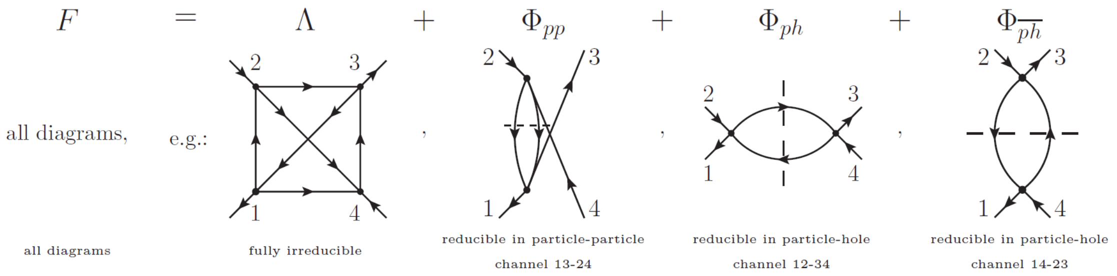
F
=
Λ
+
Φ_pp
+
Φ_ph
+
Φ_ph̄
all diagrams,
e.g.:
1
2
3
4
all diagrams
fully irreducible
reducible in particle-particle channel 13-24
reducible in particle-hole channel 12-34
reducible in particle-hole channel 14-23

Figure 2.9: Here one can see the diagrammtic decompostion of the Full Vertex F into a fully irreducible part Λ and reducible parts Φ_r for the specific channels $r = (pp, ph, \overline{ph})$ [31]

A different complementary, approach for the division computed by the parquet equation is obtained introducing another auxiliary quantity the irreducible vertex Γ_r for a certain channel r. For example, in the ph channel one has:

$$F = \underbrace{\Lambda + \Phi_{pp} + \Phi_{\overline{ph}}}_{\Gamma_{ph}} + \Phi_{ph} \tag{2.42}$$

Γ_r can be obtained from F with the help of the Bethe-Salpeter integral equation[7], where F can be seen as a sum of all connected diagrams irreducible for a certain channel r and the reducible ones. These can linked by connecting Γ_r to F via two Green's function lines [31]:

$$F = \Gamma_r + \int \Gamma_r G G F \tag{2.43}$$

2.4.1 Response functions

Response functions can be seen as a connecting link between microscopic theory and experiments, since they describe the behaviour or response of a system when an sufficiently weak external perturbation (e.g. a magnetic field) occurs. The most famous ones are the specific heat $c_v = \frac{\partial U}{\partial T}$ the isothermal compressibility $\kappa = -\frac{1}{V}\frac{\partial V}{\partial p}$ and the magnetic susceptibility $\chi = \frac{\partial M}{\partial H}$.

---

[7] It should be mentioned here that the integral symbol stands for summing up over all internal degrees of freedom [31].

Starting point is a system with a Hamiltonian of the form $\mathcal{H} = \mathcal{H}_0 + \mathcal{H}_v - \hat{A} \cdot a(t)$. The first two term are time independent, whereas the latter represents an external perturbation $a(t)$ coupled to an observable of the system $\hat{A}$. Usually experiments are designed to measure the response of the system to an external perturbation of another observable $\hat{B}$[8], which is given by the response function:

$$\langle \hat{B} \rangle_v(t) - \langle \hat{B} \rangle_0 = \int_{-\infty}^{\infty} dt \; \chi_{BA}(t - t')a(t) \tag{2.44}$$

There exist some important features of $\chi_{BA}(t - t')$ which will be briefly listed:

- Even if $\chi_{BA}(t - t')$ is time dependent it does not depend on $a(t)$ at all.
- Due to causality (effects are caused by action thus happen later in time) response functions are always retarded.

Within linear response theory (no higher order terms contribution of the perturbation) the Kubo-Nakano formula provides a simple form for $\chi_{BA}(t - t')$[9], for which in this case $\hbar$ is set to 1.(for a detailed derivation see [30]).

$$\chi_{BA}(t - t') = i\Theta(t - t')\langle [\hat{B}(t), \hat{A}(t')] \rangle_{v=0} \tag{2.45}$$

In our case calculations will be performed within the Feynman diagrammatic formalism at finite temperatures. Hence the above quantity must be expressed in imaginary times:

$$\chi_{BA}(\omega) = \int_0^{\beta} e^{i(\omega + i0^+)} \langle \mathcal{T}_\tau B(\tau) A(\tau') \rangle_{v=0} \tag{2.46}$$

Although these expressions might appear in simple form, actual calculations can become quite challenging, especially when performing the analytic continuation. Thus some special cases will be discussed now.

---

[8] indeed in many cases $\hat{B} = \hat{A}$, which does not alter the formalism

[9] This holds only for time independent Hamiltonian, which are translational invariant. Otherwise χ would have an explicit time dependence instead of a mere time difference.

U=0 limit of the Hubbard model

First let's have a closer look at the non-interacting limit. As seen in Eq. 2.46 and 2.45 the thermal average is evaluated with respect to the full unperturbed Hamiltonian $\mathcal{H}_0+\mathcal{H}_v$. If $\mathcal{H}_v = 0$, Wick's theorem can directly be applied to evaluate the resulting combination of fermionic operators and in for the paramagnetic spin susceptibility one obtains:

$$\chi_{\sigma_z\sigma_z}(\vec{q}, i\omega_m) \sim \frac{1}{\beta}\sum_{nn'}\sum_{\vec{k}}\sum_{\sigma} G_{\vec{k}\sigma}(i\nu_n)G_{\vec{k}+\vec{q}\sigma}(i\nu_n + i\omega_m)\delta_{n,n'} \tag{2.47}$$

The summation over n and n' represents the Fourier transform to momentum space where all fermionic Matsubara frequencies are summarized, whereas m are bosonic Matsubara frequencies[10], see Sec. 2.1.1. For the static case $i\omega_m \to 0$ the expression changes to

$$\chi_{S_zS_z}(\vec{q}, 0) \sim \sum_{\vec{k}}\sum_{\sigma} \frac{n_\sigma(\epsilon_{\vec{k}+\vec{q}}) - n_\sigma(\epsilon_{\vec{k}})}{\epsilon_{\vec{k}} - \epsilon_{\vec{k}+\vec{q}}} \tag{2.48}$$

which in the $\vec{q} \to 0, T \to 0$ becomes the Pauli susceptibility [30].

$$\chi_{S_zS_z}(0, 0) \sim \mathcal{N}(\epsilon_F), \tag{2.49}$$

with

$$\mathcal{N}(\epsilon_F) = -\sum_{\sigma}\frac{1}{N_k}\sum_{\vec{k}}\frac{dn_\sigma(\epsilon_k)}{d\epsilon_k}\Big|_{T=0} \tag{2.50}$$

Atomic limit of the Hubbard model

As discussed in [30] the atomic limit, which essentially treats the case $(U/t \to \infty)$ gives a Curie like expression for the static susceptibility:

$$\chi(\vec{q}, 0) \sim const \cdot \frac{1}{T} \tag{2.51}$$

---

[10] For a better readability ω will be used for bosonic frequencies and ν for fermionic ones from now on.

2.4.2 Calculation of momentum dependent response functions in DMFT

The standard procedure retrieving momentum dependent susceptibilities from DMFT, which is a crucial step in our work, will be sketched now.

- In a first step one performs a DMFT self consistency calculation of which the local Green's function and also the local generalized susceptibility are extracted from the auxiliary Anderson impurity model, i.e., they are obtained at the end of the self-consistent procedure.
- Secondly one considers the Bethe Salpeter equation (BSE) for the local AIM of DMFT

$$\chi_{AIM}^{\nu\nu'\omega} = \chi_{0,AIM}^{\nu\nu'\omega} + \chi_{0,lAIM}^{\nu\nu'\omega}\, \Gamma_{AIM}^{\nu\nu'\omega}\, \chi_{AIM}^{\nu\nu'\omega} \tag{2.52}$$

- By inverting this equation, an expression for the irreducible vertex $\Gamma_{AIM}^{\nu\nu'\omega}$ can be evaluated

$$\Gamma_{AIM}^{\nu\nu'\omega} = \beta^2 \left[\left(\chi_{AIM}^{\nu\nu'} \right)^{-1} - \left(\chi_{0,AIM}^{\nu\nu'} \right)^{-1} \right]^{\omega} \tag{2.53}$$

  where

$$\left(\chi_{AIM}^{\nu\nu'\omega} \right)^{-1} = G_{AIM}^{(2)} - G_{AIM}^{(1)} G_{AIM}^{(1)}, \tag{2.54}$$

  and

$$\chi_{0,AIM}^{\nu\nu'\omega} = -\beta G_{AIM}(i\nu) G_{AIM}(i\nu + i\omega). \tag{2.55}$$

- In a final step the BSE for the lattice is formulated in a ladder where $\Gamma_{loc}^{\nu\nu'\omega}$ is inserted, since when included in a ladder decomposition the irreducible vertex becomes purely local [13]. Additionally, the momentum dependent Green's function from DMFT $G_{DMFT}(\nu, \vec{k})$ is taken to build the momentum dependent χ_0 terms, as seen in Fig. 2.10.

$$\chi_{k,k',q}^{\nu\nu'\omega} = \chi_{k,k'q}^{0\ \nu\nu'\omega} + \chi_{k,k',q}^{0\ \nu\nu'\omega}\, \Gamma_{AIM}^{\nu\nu'\omega}\, \chi_{k,k';q}^{\nu\nu'\omega} \tag{2.56}$$

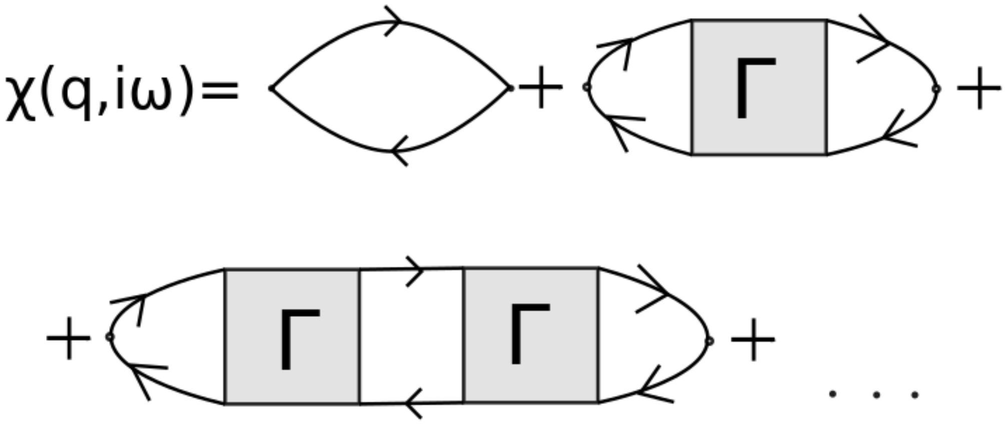

Figure 2.10: Ladder decomposition of the response function $\chi(q, i\omega)$.

- By inverting the last expression one obtains a result for the momentum dependent generalised susceptibility

  $$\left(\chi^{\nu\nu'\omega}_{k,k'q}\right)^{-1} = \left(\chi^{0\;\nu\nu'\omega}_{k,k',q}\right)^{-1} - \Gamma^{\nu\nu'\omega}_{AIM}. \tag{2.57}$$

  were the inversions are performed with respect to the fermionic variables (k, ν, k', ν') for each (fixed value) of the bosonic ones (q, ω)

- Finally to obtain the momentum dependent physical susceptibility , the internal (fermionic) frequency momentum summation must be performed:

  $$\chi(q, \omega) = \sum_{\substack{k,k' \\ \nu,\nu'}} \chi^{\nu\nu'\omega}_{k,k',q} \tag{2.58}$$

CHAPTER 3

Quantum phase transitions

In this house, we obey the laws of thermodynamics!

— The Simpsons

In this second methodological chapter the main formalism for describing and characterizing phase transitions will be introduced. Starting from classical ones, the most fundamental concepts, such as order parameters or universality classes will be concisely presented. In a second step, the whole theory will be extended to not thermally induced phase transitions, the so-called quantum phase transitions. The regions of the phase diagrams in the proximity of a quantum critical point exhibit various interesting physical phenomena, some of which will be investigated within this thesis. Their general importance will be shortly illustrated with some textbook examples. Subsequently in the next part of the chapter theories for adequately describing classical (Landau Theory) as well as quantum criticality (Hertz-Millis-Moriya Theory) will be concisely presented. In the last section eventually the most recent literature results for the classical as well as the quantum critical behaviour of the Hubbard Model will be discussed.

3.1 Classical phase transitions and criticality

Before we start with any theories or formalisms let us first define the term "phase" from a physical point of view:

"Phases can be seen as defined states of a matter distinguishable by means of clear differences in their thermal, mechanical and magnetic properties"

Transitions between different phases occur when changing a certain external control parameter, e.g. the temperature T, the magnetic field h, the chemical potential μ etc. More rigorously, the “clear differences” mentioned above correspond to a non analytic behaviour of thermodynamic potential, like the Free Energy F.

By further examining the phase transitions, two main subclasses of can be identified, for which the following table 3.1 captures the principal differences, adapted from [32].

1^{st} order phase transitions	2^{nd} order phase transitions
• 1^{st} derivative of thermodynamic potential discontinuous	• continuous 1^{st} derivative of thermodynamic potential
• latent heat $Q_L = T_0 \Delta S$	• no latent heat $Q_L = 0$
• metastable phases occur	• unsteady or divergent behaviour of response functions (χ, c_v, κ)

Table 3.1: Differences between 1^{st} and 2^{nd} order phase transitions are confronted

From now on, however, when talking about phase transitions we will stick to 2^{nd} order ones, because these exhibit the critical phenomena investigated within this thesis. In this respect, we should recall that such transitions are often accompanied by a symmetry breaking process, e.g. rotational symmetry breaking in a antiferromagnet, where the disordered high temperature paramagnetic phase changes into the ordered antiferromagnetic phase, spontaneously breaking the symmetry of its Hamiltonian. In the classical case thermal (spatial) fluctuations destroy long range order.[1] This transition can be seen by the disappearance of a so called order parameter, i.e. for the above case the magnetization $\vec{\mathcal{M}}$ at $T \geq T_N$, where T_N stands for the Néel transition temperature from a antiferromagnetic (AF) to a paramagnetic (PM) state.

In Fig 3.1 shows the generic behaviour for a typical second order phase transition is illustrated as a function of a non thermal parameter, i.e. the pressure p. For the parameter region slightly above and under (blueish in picture) T_N (brown line) scalings of several thermodynamic quantities exhibit power-law behaviors.

---

[1] The paramagnetic state for $T > Tc$ is not intended to be a non-magnetic state as assumed in the Stoner model, but it can be seen as a state where the non-interacting (or weakly correlated) individual moments still exist [33].

Table 3.2 shows the functional dependencies in case of an Ising antiferromagnetic system.

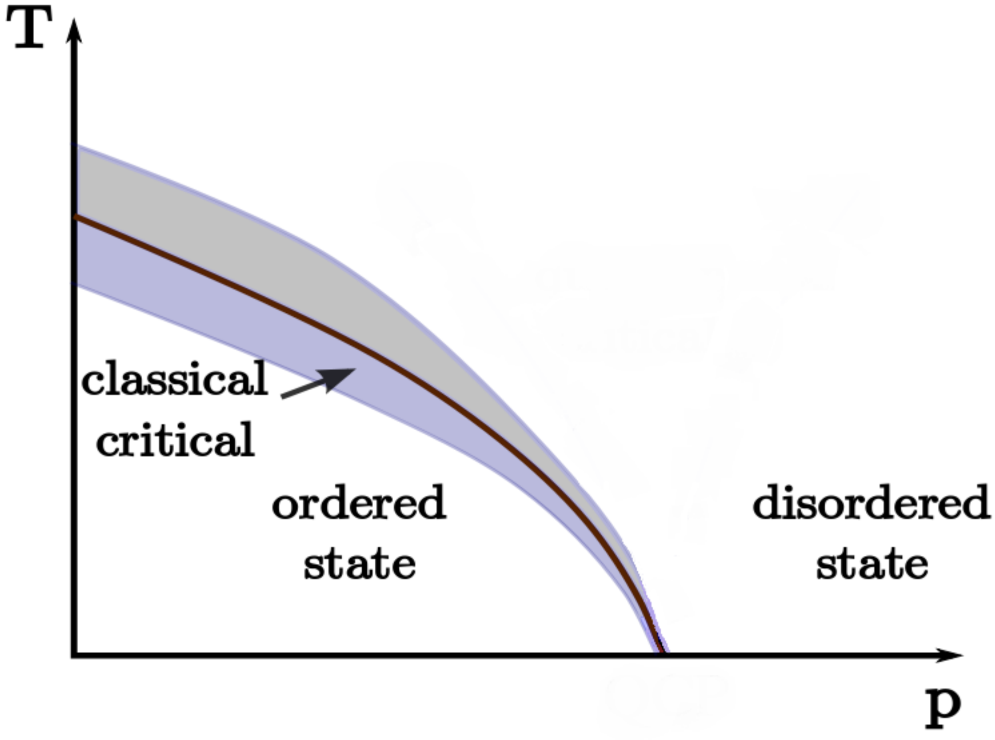

Figure 3.1: This adapted figure from [34] depicts the classical critical regime of a 2^{nd} order phase transition.

It can be immediately seen that all quantities, since $\gamma > 0,\ \nu > 0$ show a power-law divergent behaviour at $T = T_c$. As mentioned above these exponents do not depend on microscopic properties of the system but rather on macroscopic parameters like, dimensionality d of the system or the interaction range. This leads to the definition of the universality classes. These are a large collection of different systems which exhibit phase transitions with the same critical exponents, i.e. the mean field theory class[2] $\gamma = 1$ and $\nu = 0.5$.

---

[2] For finite-T (classical) phase transitions, DMFT belongs to this class which will be discussed in more detail in 3.3.1.

thermodynamic quantity	scaling relation
specific heat c_v	$c_v \sim \left\|\frac{T-T_c}{T_c}\right\|^{-\alpha}$
order parameter m	$m \sim \left\|\frac{T-T_c}{T_c}\right\|^{\beta}$
susceptibility χ	$\chi \sim \left\|\frac{T-T_c}{T_c}\right\|^{-\gamma}$
correlation length ξ	$\xi \sim \left\|\frac{T-T_c}{T_c}\right\|^{-\nu}$

Table 3.2: Scaling relation for the critical exponents $\alpha, \beta, \gamma, \nu$ for a magnetic system are shown

3.2 Quantum criticality

As one can see in Fig. 3.2, which has been adapted from the original Fig. 3.1, for a certain value of the (non-thermal) control parameter $p = p_c$ the temperature of phase transition can vanish ($T_c = 0$). For higher values of p, thus, no ordered state can be found. This means that for the isothermal $T = 0$ line nonetheless a phase transition occurs. Of course this one is not driven only by spatial or thermal fluctuations but also by quantum or temporal ones. Intuitively, one would also assume that for $T = 0$ particles would rest, which due to uncertainty principle is not possible and could be seen as a confirmation of the existence of quantum fluctuations. These might progressively suppress the long range order.

At this point, one might pose argument formulated within the 3$^{\text{rd}}$ law of thermodynamics which essentially states: "It is impossible by any procedure, no matter how idealized, to reduce the temperature of any closed system to zero temperature in a finite number of finite operations." [35][3] This would reduce the problem and its consequential physic to a merely $T = 0$ academic problem.

If we recall the Tab. 3.2, another important parameter describing the classic phase transitions is the correlation length ξ. Now we shall briefly refresh this concept in an short intermezzo

---

[3] In graduate physics course my teacher Prof. Aumayr once explained this law with the statement of a former student of him: "We cannot win the game" which I think captures the quintessence of the law.

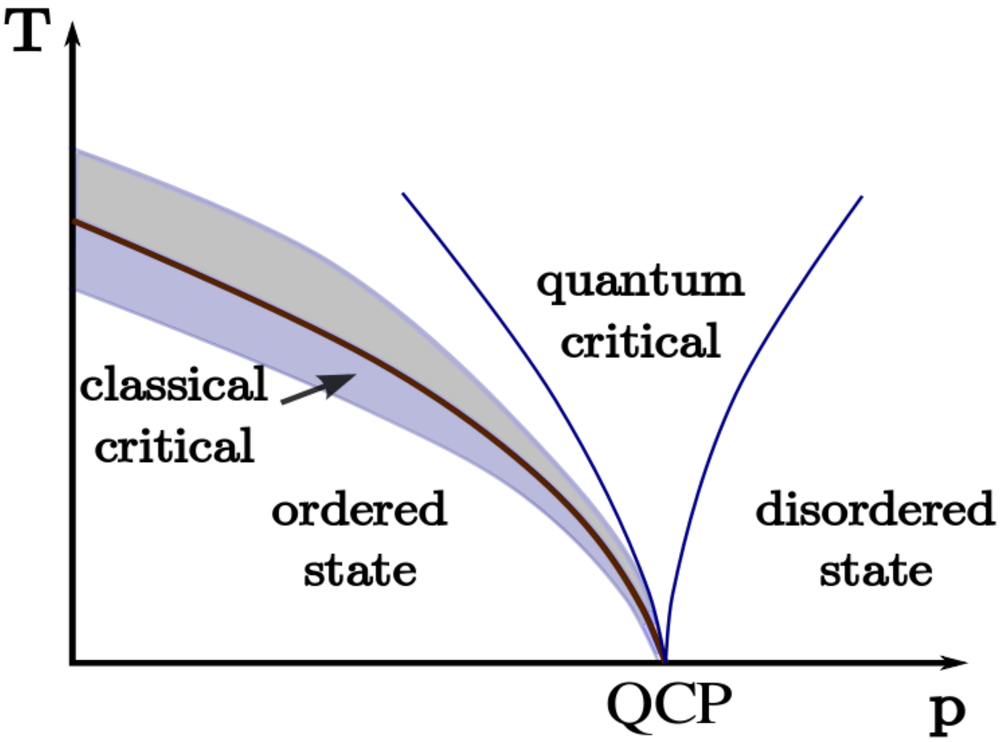

Figure 3.2: This figure from [34] depicts the phase diagram region of quantum critical behaviour, where temporal fluctuations are dominant.

Intermezzo for spatial fluctuations

Remembering the general expression for (electronic) correlations $G(\vec{r})$ [32]:

$$G(\vec{r}) = \langle \varphi(\vec{r})\varphi(0)\rangle - \langle \varphi(\vec{r})\rangle\langle \varphi(0)\rangle. \tag{3.1}$$

In a bulk (3D) system, correlations are connected to the correlation length via the following relation:

$$G(\vec{r}) \sim \frac{e^{-|\vec{r}|}/\xi}{|\vec{r}|} \tag{3.2}$$

The expression in Tab. 3.2 for ξ shows that for $T \to T_c$ its values goes to ∞, which is a general feature of second order phase transitions. The "energy scale" of these has the order of magnitude $\sim k_B T_c$

After this introduction of $\xi = \xi_r$ [4] we will now have a look at the correlation length of temporal (quantum) fluctuations. These depend on temperature $\xi_t \sim T^{-\nu}$, but more important they can be linked also on non-thermal control parameters (i.e. pressure p) [2]:

$$\xi_t = |p - p_c|^{-z\nu} , \tag{3.3}$$

where z is the so called dynamical critical exponent, which will be explained in 3.3.2.

When looking again at Fig. 3.2 in the quantum critical region inside the blue lined cone $1/\xi_t << \xi_r$ holds and the effects of the presence of the quantum critical point need to be considered in this parameter region. On the other hand, in the so called "(quantum) disordered stated where $1/\xi_t >> \xi_r$ they can be safely neglected.

A remarkable experimental realization of this schematic phase diagram has been found by J. Custers et al. [36]. They showed that for the heavy fermion compound $YbRh_2Si_2$ using a transversal magnetic field B as non thermal parameter a different behaviour for the low-temperature resistivity emerges. Fig. 3.3 illustrates the situation, where in the orange funnel shaped region the usual, Fermi-liquid $\rho(T) \sim \rho_0 + AT^2$ changes to a linear one $\rho \sim \rho_0 + BT$.

3.3 Theories for phase transitions

After this rather phenomenological section, now two theories for characterizing classical phase transitions, the Landau theory and its respective counterpart the Hertz Millis Moriya (HMM) extending theory for quantum phase transitions will be introduced formally now.

3.3.1 Landau Theory for classical phase transitions

In 1938 the Russian physicist Lew Landau formulated for the first time a theory for 2nd order classical phase transitions, by recognizing in the symmetry breaking processes a crucial point. On the basis of this consideration he formulated the following assumptions, which have been adapted from [32].

- A phase transition is characterized by an order parameter φ or its respective density $\psi(\vec{r})$.

---

[4] In order to avoid misunderstandings the subscripts r denotes the spatial correlation length

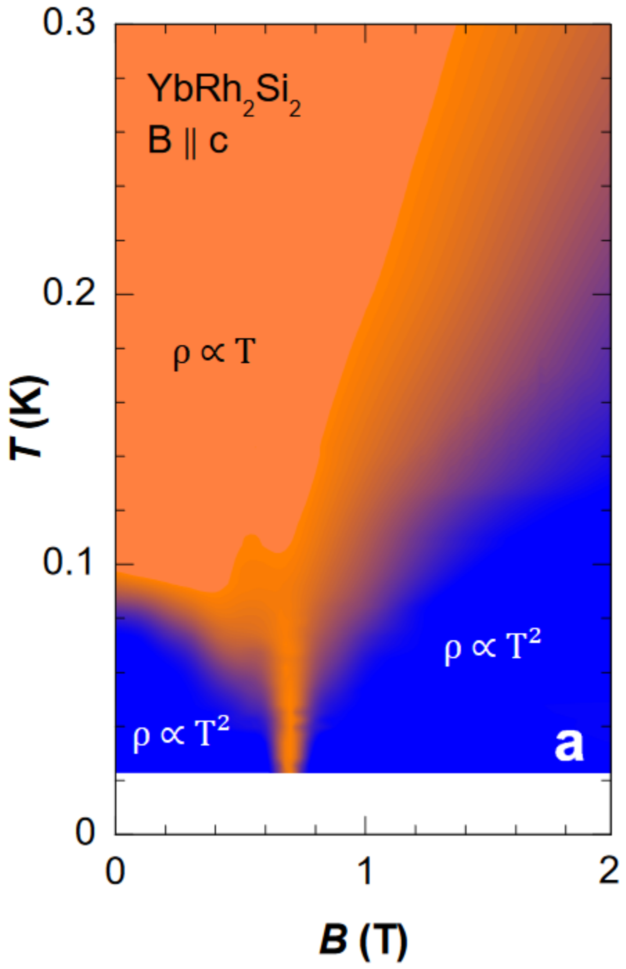

Figure 3.3: This figure from [36] shows the "high temperature" properties of a QCP, which perfectly matches the schematization of Fig. 3.1.

- The free energy $F(T, h)$ explicitly depends on an external field (i.e. the Magnetic field) and its first derivative $\frac{\partial F}{\partial h}$ defines the order parameter.
- For $T \lesssim T_c$ the order parameter φ is so small that the free energy is expanded in terms of it. Due to the fact of invariance of F under symmetry transformations in case of h=0, only even powers of φ survive and temperature dependence is captured in the respective constants:

$$F(T, \varphi) \approx F_0(T) - h\varphi + a(T)\varphi^2 + b(T)\varphi^4 + ... \tag{3.4}$$

Evaluating the expression in Eq. 3.4 for the equilibrium state, where the free energy is in a minimum we obtain the following results for the order parameter in case of no external field:

for $a(T) > 0$:

$$\varphi = 0 \tag{3.5}$$

for $a(T) < 0$:

$$\varphi = \pm\sqrt{\frac{-a(T)}{2b(T)}} \tag{3.6}$$

Hence, as Landau observed, the minimal qualitative description of a 2^{nd} order phase transition can be obtained by assuming the the temperature dependence of a and b is simply given by $a \approx a_0(T - T_c)$ and $b \approx b_0 > 0$[5]: we see the three different cases for $T \gtrless T_c$ and $T = T_c$ illustrated in Fig. 3.4. For temperatures above T_c there is only on minimum of f for a disappearing order parameter $\varphi = 0$ (dotted line), whereas for temperatures below T_c there exist two symmetric, with respect to origin, with a non-zero φ (dashed line).

As we will show now the Landau theory is essentially a good description for mean field approximation. We show thus explicitly, as an example, the the critical exponent γ controlling the critical behaviour of the susceptibility $\chi \sim \left|\frac{T-T_c}{T_c}\right|^{-\gamma}$. The following derivation has been adapted from [32]. Starting point is again the standard definition of the susceptibility (ie of the magnetic system):

$$\chi = -\frac{\partial^2 F}{\partial h^2} = \frac{\partial \varphi}{\partial h}\bigg|_{h=0} \tag{3.7}$$

Differentiating Eq. 3.3.1 with respect to φ and minimizing the expression we get:

$$2a_0(T - T_c)\varphi + 4b_0\varphi^3 = h \tag{3.8}$$

After performing another derivate with respect to h and inserting the definition of 3.7 an expression for the susceptibility can be found

---

[5] This constant has to be always positive in order to guarantee the existence of a global maximum

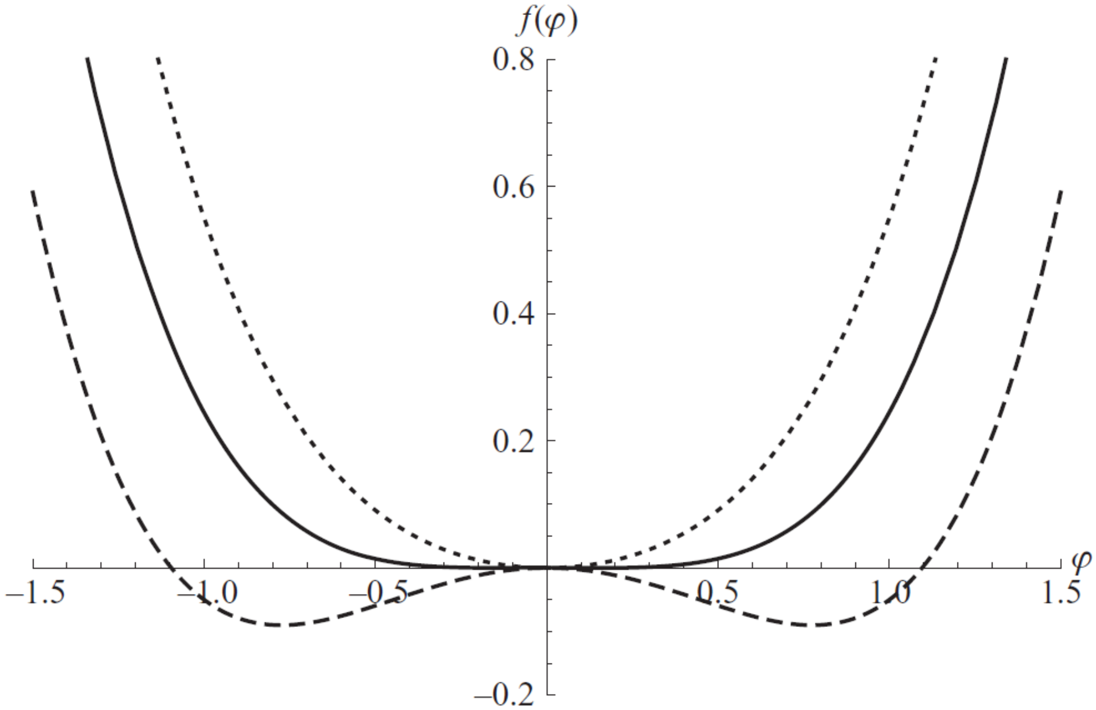

Figure 3.4: The dotted line show the functional behaviour of the free energy per Volume f for $T > T_c$, the continuous one for $T = T_c$ and the dashed one for $T < T_c$

$$\chi = \frac{1}{2a_0(T - T_c) + 12b_0\varphi^2} \tag{3.9}$$

Exploiting the relations of Eq. 3.5 and 3.6 we obtain a final expression for χ:

$$\chi \begin{cases} \frac{1}{2a_0(T-T_c)} & T > T_c \\ \frac{1}{4a_0(T_c-T)} & T < T_c \end{cases} \tag{3.10}$$

It can be seen for $T = T_c$ the susceptibility diverges corresponding with a critical exponent $\gamma = 1$ both above (γ) and below (γ') T_c, which in fact coincides with the mean field exponent. Analogous results for the critical behaviour of the correlation length or the order parameter itself can be found. It should be recalled at this point that Landau theory completely neglects all spatial correlation (which explains the circumstance of its mean field “character”). This may lead to quantitative discrepancies for phase diagram region in immediate vicinity of a critical point/line if the dimensionality of the system or the range of the interaction are not large enough. For example DΓA which goes a step beyond DMFT including spatial correlations will be, in general, not describable with the Landau theory.

While having now talked about model theories for classical phase transitions we in a next step we will have a brief look into the conventional theory for the quantum case, which can be qualitatively understood as an inclusion of quantum fluctuations within the Landau formalism.

3.3.2 Hertz Millis Moriya Theory for quantum criticality

Roughly 40 years after the pioneering work of Lev Landau. John Hertz published a scientific review which investigated phase transition at zero temperature [37]. He came to the conclusion that the Landau formalism for describing classical phase transition can be extended by taking into account the time as additional dimension. This approach can be motivated by the fact that while in the classical statistic description spatial configuration are crucial whereas in the quantum case the weight is expressed through the Schrödinger factor $e^{-i\mathcal{H}t}$. As mentioned in the last section at any phase transition the correlation length diverges, however, at a QCP also the correlation time ξ_t shows a similar behaviour with respect to the critical doping n_c [2]:

$$\xi_t \sim |n - n_c|^{-z} \tag{3.11}$$

resulting into an effective dimension:

$$d_{eff} = d + z \tag{3.12}$$

Now one could naively assume that $d_{eff} = d+1$. However, in general the problem is more complex than simply taking only time as an additional dimension. Hertz who mainly investigated itinerant electron systems by renormalization group methods could show that z depends on the scaling between spatial an temporal fluctuation. For instance in case of insulators one finds z=2 and for metals z=3 [2]. On the other hand, important limits of applicability of this “conventional” theory have emerged in the last 40 years (wrong order of phase transition, wrong description for certain compounds which show a heavy fermion behaviour). In fact several attempts to save this theory have been made, among which we recall the most famous one by Millis who extended the scaling relation equation for temperature [38]. Furthermore, we also recall the Moriya’s extensions of the theory for describing magnetic materials with strong spin fluctuations outside the quantum critical region. [38]

Despite this progress some drawback could not be overcome. Since it is based on renormalization group treatment it can be seen as a perturbative approach to the problem thus making its application more problematic for strong coupled systems. Another important aspect is the complete neglection of Fermi surface features of the compound (in the next chapter we will see that these will be a crucial factor for the failure of HMM for the 3D Hubbard model in the quantum critical region).

3.4 Criticality by means of the Hubbard model

3.4.1 Classical criticality for the HM

After introducing and discussing the generic formalisms for characterizing the classical and the quantum criticality, now a closer look will be given to the critical behavior of the model of interest in this work: the 3D Hubbard Model. As a first step, we consider the n=1 half-filled case and briefly resume the main results of Refs. [39], [40]. Fig 3.5 illustrates the variation of the Néel temperature T_N for different interaction strengths U computed in DMFT and its extensions. This critical temperature is determined by the divergence of the momentum dependent spin susceptibility $\chi(\omega, \vec{Q})$ (for which the “extraction” process within DMFT is sketched in Sec. 2.4.2) computed at the underlying ordering vector, which corresponds to $\vec{Q} = (\pi, \pi, \pi)$ in case of half filling. One can immediately draw several crucial conclusion from this picture.

Starting from weak-coupling regime, we see a first significant increase of T_N For small values of U, T_N displays a “renormalized” mean-field (exponential) behavior, see [41], [42], [43]. This gets gradually weakened by increasing U resulting in a maximum around $U \approx 2$. We observe that in general the DMFT and the DΓA Néel temperature are deviating from each other since in DΓA the additional space correlations (here AF correlations) further suppress the ordering tendency of the system. The significant deviation of DΓA from a mean-field description is also visible in the T-behavior of the critical properties illustrated in Fig 3.6, where the inverse antiferromagnetic transition susceptibility computed in DΓA is plotted for several U values. In fact the χ^{-1} significantly differs from a linear mean field behavior in a T interval, which becomes larger at intermediate U due to the higher impact of spatial correlations in this regime. [6]

---

[6] For the work performed in this thesis scaling for t=1 has been chosen in contrast to $1/2\sqrt{6}$ previous studies shown here (including T. Schäfer’s work discussed later) meaning that quantities like the interaction strength U, the temperature T and its inverse β have to be multiplied (or divided) by this pre factor.

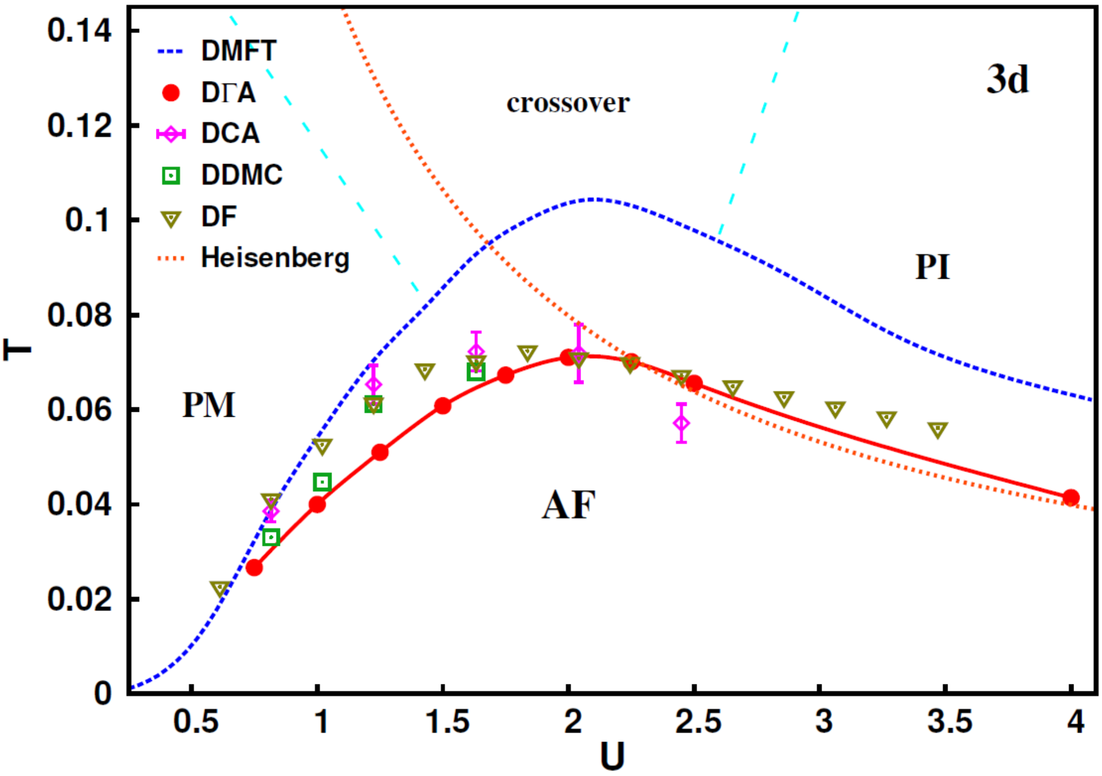

Figure 3.5: This picture (taken from [40]) shows the Néel Temperature of the 3D Hubbard Model as a function of the interaction strength U (in unit of $2\sqrt{6}t = 1$) for DMFT and its diagrammatic extensions as well as (for comparison) the ones of the Heisenberg model.

Eventually for $U > 2$, the DΓA results are approaching rather precisely the quantitative behaviour of the Heisenberg model (HBM), where T_N decreases with U. A similarity was also recognized for the scaling relations of the susceptibility as well as for the correlation length which in both the 3D HBM and DΓA gets larger than the corresponding mean-field value. Similar trends have been also obtained in dual-fermion (DF) [44]. This is in contrast to DMFT, which besides overestimating T_N, always yields mean-field critical exponents ($\gamma = 1$ and $\nu = 0.5$): DMFT is a pure mean-field from the point of view of spatial correlations.

It shall be also mentioned, that DMFT and DΓA (within the precision of numerical data) obey the Fisher relation:

$$\frac{\gamma}{\nu} = 2 - \eta \tag{3.13}$$

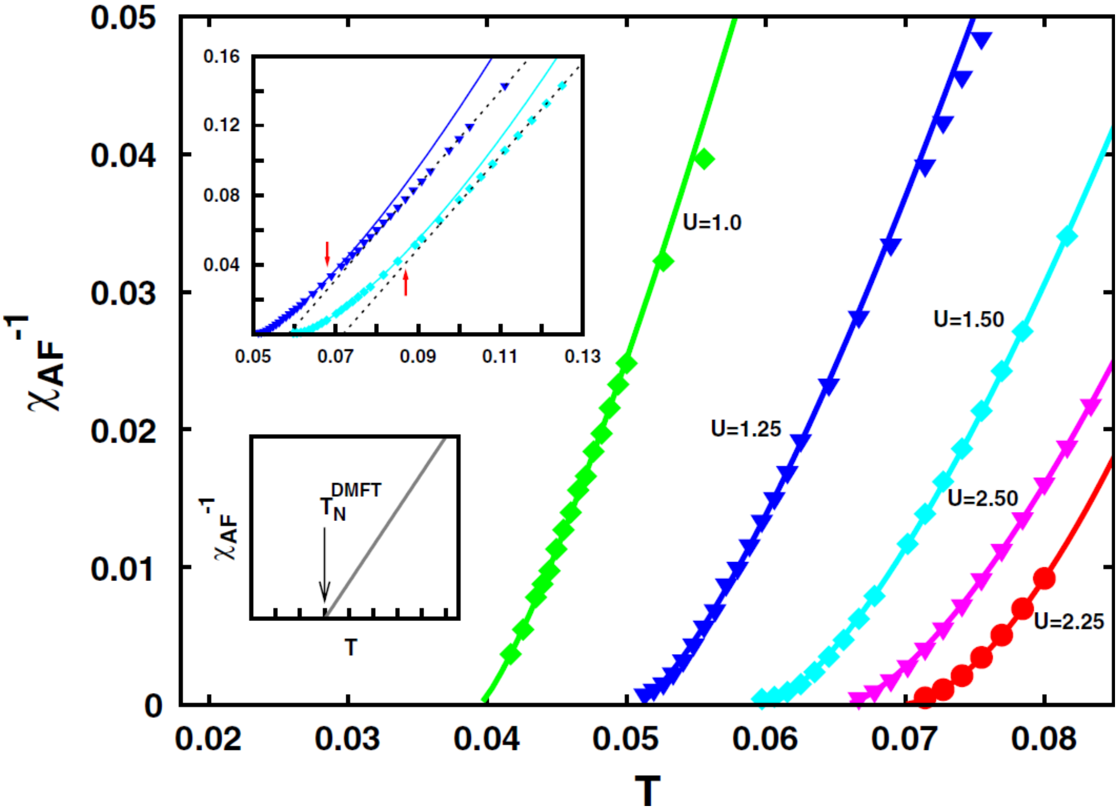

Figure 3.6: This picture (taken from [39]) shows the inverse susceptibility for different values of U. In the lower inset a linear mean field (DMFT) behaviour is shown, while in the upper one the deviation between DΓA and DMFT behaviour is zoomed in for U=1.25 and U=1.50.

As pointed out in [45] in any case for the three dimensional systems considered here, the anomalous exponent η, which vanishes completely for higher dimensions than the upper critical one, is typically neglected. For DMFT, a mean-field theory in space, η is always zero.

It is also important to recall recent studies by *L. del Re et al.* which investigated the attractive Hubbard model out of half filling [46] by means of DΓA: Fig. 3.7 show numerical fit of the particle-particle susceptibility taking into account sub-to-leading orders, see also [47]. This refined analysis demonstrates that DMFT yields for the superconducting phase transition mean-field classical critical exponents, while ladder DΓA calculations, with momentum independent Moriya corrections [48], [40], yields the exponents to understand spherically symmetric classes (i.e.:$\gamma = 2, \nu = 1$) analogously to the two particle self-consistent (TPSC) approach [49], [50]. As the spherically symmetric model corresponds to the universality class (N=∞, finite d), this is in contradiction to expected 3D-XY model ones. Tab. 3.3 shows the comparison between values of different universality classes and the results computed in DΓA by *L. del Re et al.* [46].

Further investigation will be needed to carried out whether a refinement of the critical exponents o DΓA can be obtained by means of momentum dependent Moriya corrections [40] or by an explicit/fully self-consistent ladder-DΓA algorithm.

	$d=\infty$ (Mean-Field)	$O(1)$ (Ising)	$O(2)$ (XY)	$O(3)$ (Heisenberg)	$O(\infty)$ (TPSC)	ladder-DΓA SC	ladder-DΓA CDW	ladder-DΓA AFM
ν	1/2	0.63	0.67	0.71	1	0.98	0.86	0.72
γ	1	1.23	1.33	1.38	2	1.9	1.79	1.41

Table 3.3: This table, taken from [46], show the values for critical exponents of different universality classes compared to results obtained by ladder-DΓA (the results for ladder-DΓA AFM, however, have been taken from [39])

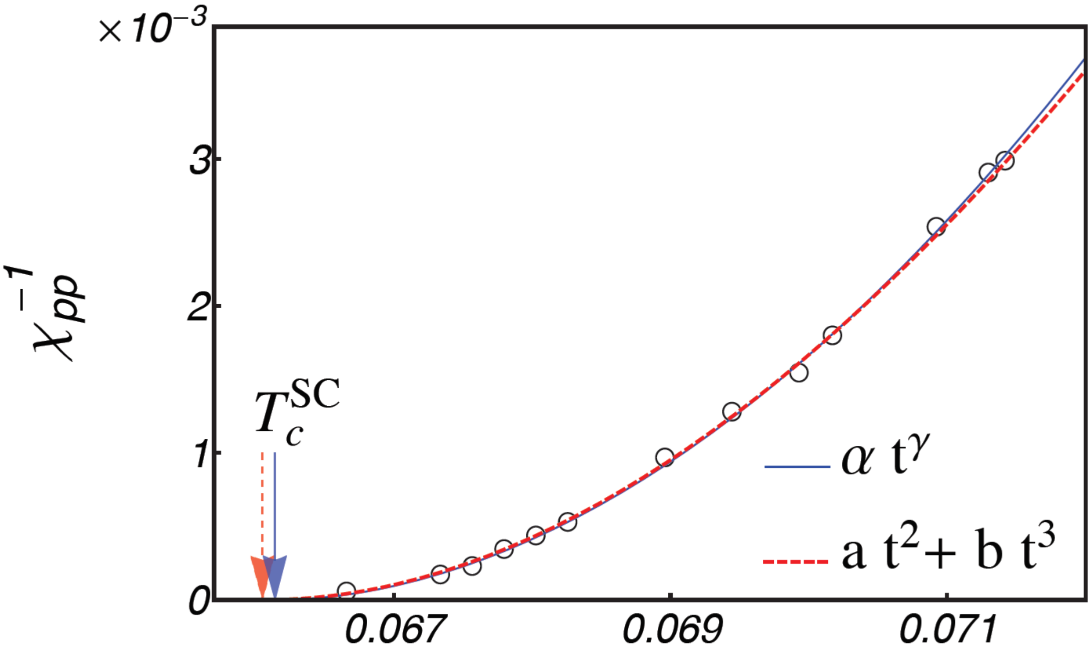

Figure 3.7: This figure taken from [46], show the comparison between two numerical fits for the inverse particle-particle susceptibility. The red-dashed line, which takes sub-to-leading order into account show a slightly lower critical temperature. The latter seems in better agreement with the remarkably different critical exponents

It should be pointed out here, that DΓA results for critical exponents are always obtained by numerical fits of data which are limited to regions with a finite distance with respect to the calculated critical temperature. As described by the work of Tremblay [47], where he pointed out that including sub-to-leading order might be necessary for controlling the intrinsic uncertainty of this fitting procedure [45], this circumstance may result in missing information of "last minute" changes in the curvature of data in proximity to T_c. For this reason in the work by *L. del Re et al.* both fitting procedures were adopted (see Fig. 3.7). Nevertheless, the steady computational physics progress of the last years will progressively mitigate this kind of issues.

3.4.2 Quantum critical Hubbard model out of half filling

In the following paragraphs we will focus again on the repulsive Hubbard model in 3D. This time, however, we will leave the n=1 density "cut" in order to systematically approach the critical doping $\delta_c = 1 - n_c$ where a QCP occurs. It should be mentioned briefly here that, when talking about doping the system, we have considered the case of hole doping. The main results and conclusions of the work by *T. Schäfer et al.* [51] will be explicitly presented below, as they provide the main motivation for the work performed within this thesis.

Schäfer et al. examined the three dimensional Hubbard by DΓA. As starting point the interaction U=2 (or respectively 9.789) has been chosen, since for this value the second order phase transition Néel temperature exhibits its maximum, as seen in Fig. 3.5. In Fig 3.10 the four most interesting phase diagram cuts are shown. For n=1 the same results, both for T_N and the critical behaviour ($\gamma = 2\nu, \gamma > 1, \nu > 0.5$), as obtained in [39], could be confirmed.

In the small doping regime the numerical values of ν and γ remain quite stable, however as it could be seen in the second column of Fig 3.10 a a certain hole doping level a more complicate T-dependence is seen. This results from the competition of a second incommensurate $\vec{q}$-peak different from the one at (π, π, π). This circumstance will be treated in a more detailed manner when discussion the DMFT results in chapter 4.

By reducing further the density, at about $n = n_c \approx 0.8$ (where T_N vanishes) the values of ν and γ change significantly from the 3D Heisenberg ones, *but* also from the Hertz-Millis-Moriya ones ($\nu = 0.75, \gamma = 1.5$). In fact, the peculiar values of the DΓA exponents ($\nu \approx 1, \gamma \approx 0.6$), appear to strongly violate the Fisher relation of

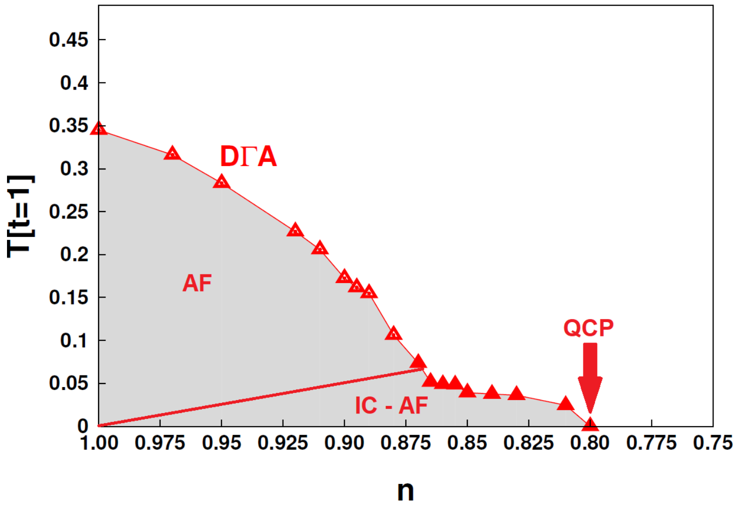

Figure 3.8: This figure, adapted from [3], shows the Néel-Temperature as a function of the doping concentration. For a critical density $n = n_c \approx 0.8$. The Néel temperature vanishes, marking the existence of a quantum critical point.

Eq. 3.13. This unexpected behavior has been ascribed to the geometrical properties of the underlying Fermi surface: the so-called of Kohn anomalies, such as Kohn points or Kohn lines, which are shown in Fig. 3.9. In general the Kohn points are a generalization of the nesting/Van Hove properties of highly symmetric Fermi surfaces. Kohn points are defines as the points of the FS that (i) are connected by the commensurate/incommensurate vector $\vec{Q}$ and (ii) have opposite Fermi velocities.

As it was explicitly shown by hands on RPA calculations in the Appendix of [51], the presecne of Kohn lines can strongly affect the values of the quantum critical exponents. For the case of KOhn lines, relevant here, one finds $\gamma = 0.5, \nu = 1$.

In fact the main aim of this work is to confirm the very same unusual quantum critical behavior for the more general case of DMFT calculations of magnetic transitions in correlated metals. If confirmed this result could have an important impact for the calculations of metallic QCP in realistic cases.

Finally when looking at a region beyond the QCP, which is shown in the last column of 3.11 a Fermi liquid behavior with finite susceptibility for zero temperature can be identified. Here the numerical fit has been performed for point situated in the quantum critical cone shaped regime,see Fig 3.2, where the results are similar to ones at the QCP.

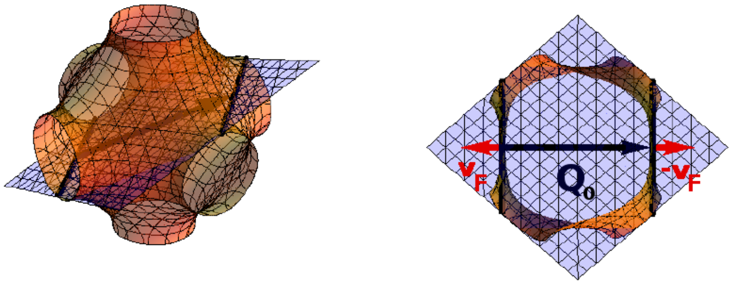

Figure 3.9: In this picture, taken from [51], Kohn lines in the 3D Fermi surface of the simple cubic lattice, with assumed nearest-neighbor hopping (left) are shown. In the right panel a 2D cut of the left picture including the SDW vector $\vec{Q}_0$ can be seen.

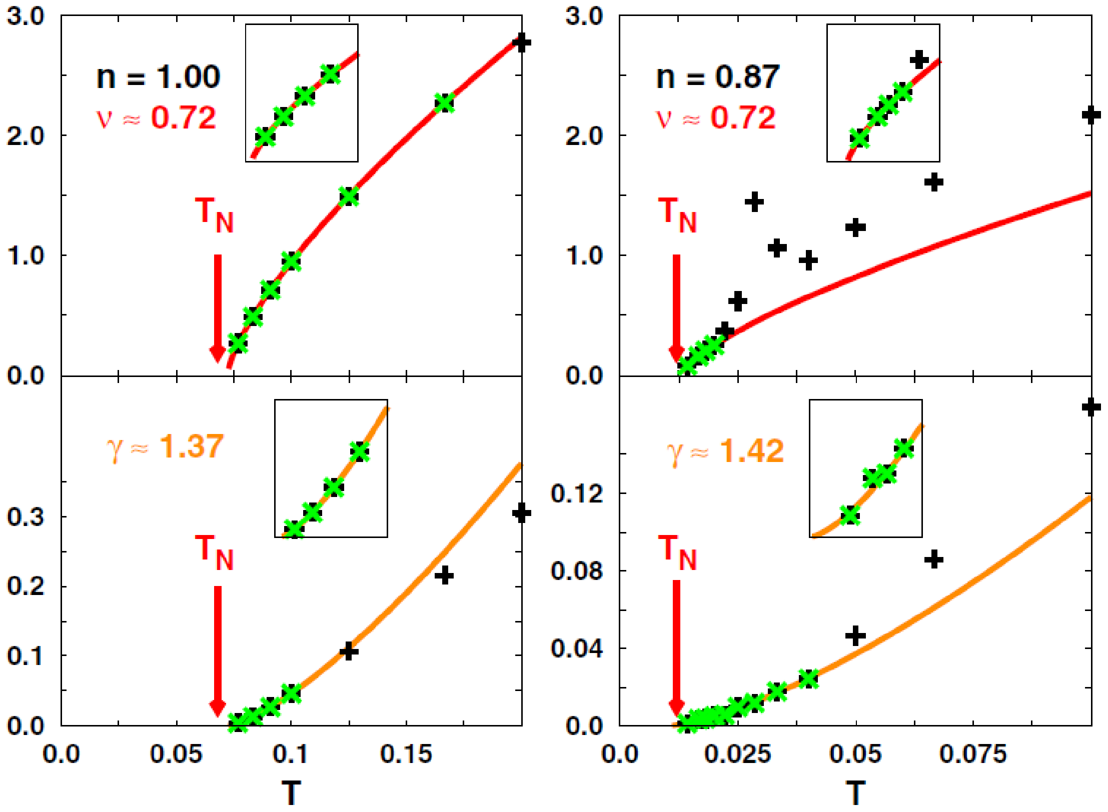

Figure 3.10: This figure which has been taken from [51] show the inverse correlation length ξ^{-1} in the upper row as well as the inverse susceptibility χ^{-1} for n=1.0 and n=0.87. For the fitted functions the green points have been considered.

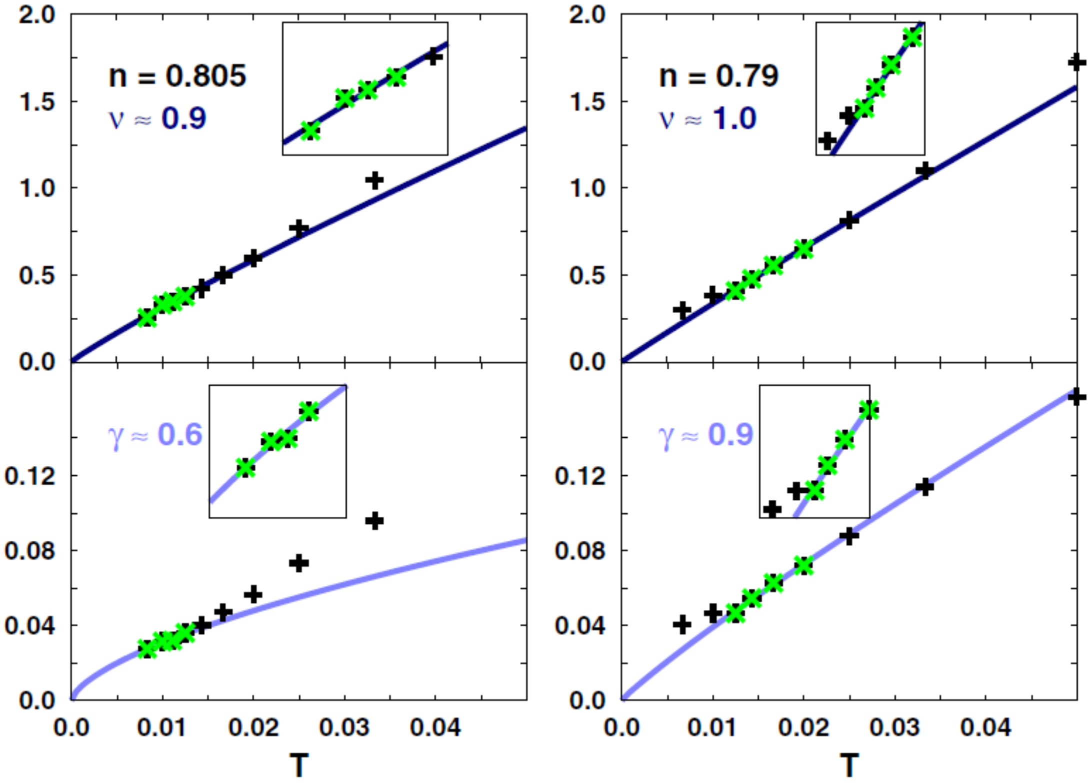

Figure 3.11: This figure which has been taken from [51] show the inverse correlation length ξ^{-1} in the upper row as well as the inverse susceptibility χ^{-1} for n=0.805 and n=0.79. For the fitted functions the green points have been considered.

CHAPTER 4

Phase Diagram and quantum criticality: DMFT results

How wonderful that we have met with a paradox. Now we have some hope of making progress.

— Niels Bohr

In this chapter the Hubbard model in three dimensions is investigated by means of the dynamical mean-field theory (DMFT). As a first step calculations are performed for the half filling (n=1.0) case: Here the magnetic susceptibility's and correlation length's temperature dependence is examined. Successively by varying the filling (hole doping) the magnetic transitions and its corresponding classical critical regions are analyzed: the critical exponents of the emerging incommensurate magnetic transition regimes are explicitly determined. By continuing the doping process the ordering temperature is suppressed until a quantum critical transition is reached. The physical properties of the QCP will be investigated more closely, to test whether they show significant deviations from expected Hertz-Millis-Moriya theory predictions. In particular the obtained numerical results are examined in the context of the possible relation with the Kohn points on the Fermi surface, already discussed in the context of and DΓ*A and RPA*

4.1 General determination process for critical exponents

Before we start discussing our DMFT results let us first briefly resume the main workflow for the numerical evaluation of critical exponents. The main algorithmic steps are:

- Step 1: A DMFT calculation is performed until convergence is reached (e.g. for the impurity lattice self energy and the chemical potential). In this thesis the *w2dynamics* code [27], which is based on CT-HYB see Sec. 2.3.2, has been used for such calculations.
- Step 2: The results from fully converged DMFT runs have been used as input for a so-called "statistical" DMFT cycle from which the local one and two particle Green's function (of the auxiliary AIM of DMFT) as well as the generalized local susceptibility can be extracted.
- Step 3: In order to obtain an expression for the physical susceptibility. An adapted Fortran module code from *T. Schäfer* which has been successfully used in [3] was utilized. As input the two particle Green's function G^2_{AIM} and susceptibility χ_{AIM} from the auxiliary AIM are needed and the irreducible vertex Γ_{AIM} is extracted by the inversion of the BSE of the impurity. Subsequently the momentum dependent susceptibility $\chi(q)$ is obtained in a direct way by the BSE of the lattice, where the detailed calculation see Sec. 2.4.2.
- Step 4: The output data for the physical susceptibilities is now utilized for a fit of the correlation lenght ξ by exploiting usual Ornstein-Zernike relation

  $$\chi(\omega = 0, \vec{q}) = \frac{A}{(\vec{q} - \vec{Q})^2 + \xi^{-2}} \tag{4.1}$$

  In addition to fitting ξ, the maximum peak at $\vec{Q}$ must be fitted too. As mathematical method the least square fitting procedure has been used as in [3].
- Step 5: The results of Step 3 and 4 are obtained for a finite number of Matsubara frequencies, due to time limits of the computational algorithms. Computations of Step 3 have to be repeated with different values of Matsubara frequencies n_ω of the interval $[-\omega, \omega]$ with $\omega = \frac{\pi}{\beta}(2n_\omega + 1)$.
- Step 6: Eventually all n_ω dependent frequencies results for a phase diagram point are extrapolated for $n_\omega \to \infty$ by the following function:

$$h(n_\omega) = a_0 + \frac{a_1 1}{n_\omega} \tag{4.2}$$

The value of a_0 will now yield the actual numerical value for a specific quantity (either $\chi, \xi, \vec{Q}$ or A) Fig. 4.1 shows schematically the extrapolation process.

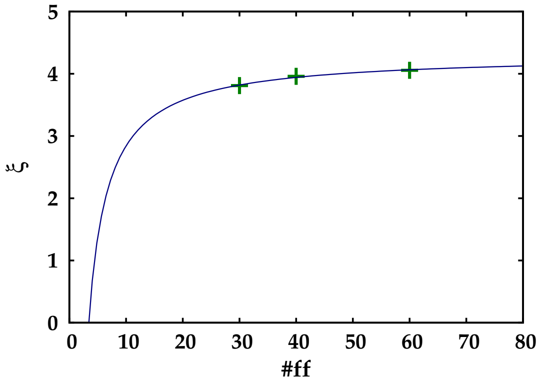

Figure 4.1: This figure illustrates the fit for the correlation length frequency extrapolation for n=0.825 and $\beta = 10$. The x-axis show the number of fermionic frequencies used for the calculations of Step 3.

Doping n	Matsubara frequencies n_ω
1.0, 0.9, 0.850, 0.825	60, 40, 30
0.8	120, 100, 80, 60
0.7885	150, 125, 100, 80
0.775	120, 100, 80

Table 4.1: This table shows the Matsubara frequencies used for each a determined doping in this work.

4.2 Classical criticality parameter regions

Half filling n=1.0

As anticipated we start by having a closer look at the half filled state n=1 for U=9.789, see Sec. 3.4 for the choice of this specific U value. Fig. 4.2 shows a fit (see Eq. 4.3 for an expression of the function) for the inverse susceptibility as well as for the correlation length. Close enough to the transition as expected, the results clearly show an evident mean-field behaviour with $\gamma \approx 1$ and $\nu \approx 0.52$. At this filling the Néel-temperature is $T_N \approx 0.48$ indicating no QCP in close proximity. The transition temperature has been calculated via the fitting functions with:

$$f(T) = B \cdot (T - T_N)^{\gamma} \qquad g(T) = C \cdot (T - T_N)^{\nu} \tag{4.3}$$

which yield consistent results.

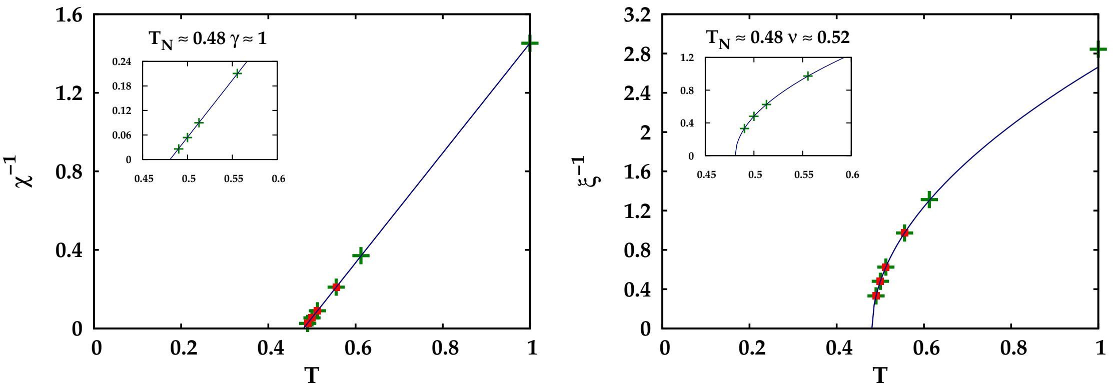

Figure 4.2: This figure shows the maximum values inverse susceptibility χ (left) and the inverse correlation length ξ (right), as a function of temperature, for n=1.0. The fitted blue lines have been used for obtaining numerical values of the critical exponents γ and ν. Only low-temperature points have been used for the fit (red dots as well as insets). This procedure has been repeated for all dopings.

At this commensurate order regime the susceptibility displays its maximum value at the wave vector $\vec{Q} = (\pi, \pi, \pi)$, indicating a commensurate (G-type) antiferromagnetic transition.

Out of half filling commensurate at order n=0.9

Fig. 4.3 shows a fit for the inverse susceptibility as well as for the correlation length, for the case of 10% hole doping (n=0.9). Here again results are mean-field like with $\gamma \approx 1$ and $\nu \approx 0.53$. However, the ordering temperature has dropped now to significantly smaller value ($T_N \approx 0.3$) than for n=1.0. At the same time, we are still in the region of commensurate magnetic fluctuations, since χ has its maximum at the wave vector $\vec{Q} = (\pi, \pi, \pi)$.

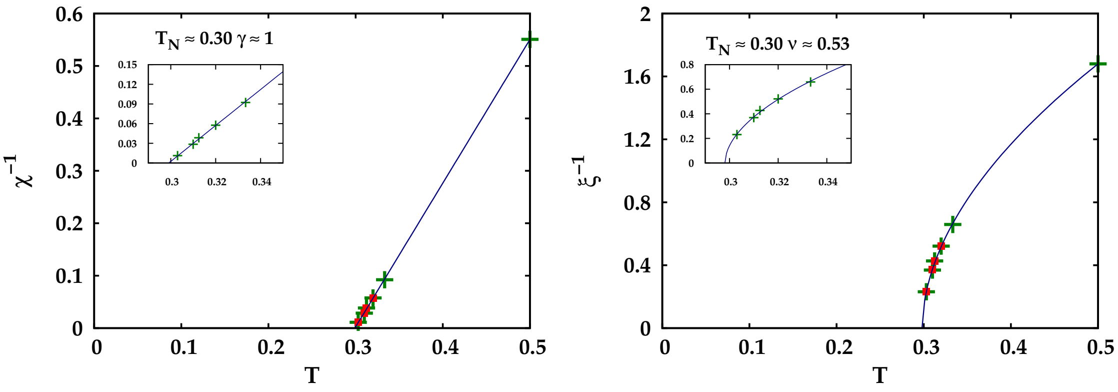

Figure 4.3: This figure shows the maximum values inverse susceptibility χ (left) and the inverse correlation length ξ (right), as a function of temperature, for n=0.9.

Incommensurate order at n=0.850 and n=0.825

By further increasing the (hole) doping of the system (n=0.850), we find the results presented in Fig. 4.4, where we plot the inverse susceptibility, the correlation length as well as their respective fits. While the critical behavior still remains mean-field like with $\gamma \approx 0.99$ and $\nu \approx 0.5$, for the inverse correlation length at intermediate temperatures apparent deviations from the mean-field behavior can be noted. In fact, they result from the emergence of another (incommensurate) peak in the susceptibility other than the antiferromagnetic commensurate one at $\vec{Q} = (\pi, \pi, \pi)$.

As it can be seen in Fig. 4.5 at high temperatures a plateau emerges between the two peaks at (π, π, π) and $(\pi, \pi, \pi - \delta q_z)$. While reaching lower temperature regions the peak at $(\pi, \pi, \pi - \delta q_z)$ becomes more pronounced while the one at (π, π, π) progressively suppressed. A similar evolution of the susceptibility has been also observed for DΓA results in [3]. This crossover affects the functional behavior of the inverse susceptibility (inset of right panel of Fig. 4.4) as discussed in [3], which indicated a smooth evolution from an antiferromagnetic to a spin density wave (SDW) phase transition.

Another interesting observation is the following: at n=1.0 and n=0.9 the behavior of the susceptibility displays a certain degree of symmetry in the q_x, q_y plane of the Brillouin Zone (not explicitly shown here, but it has the same form as for the left top picture in Fig. 4.5), at lower dopings and low-temperatures as an hallmark of incommensurate fluctuations the $(\pi, \pi, \delta q_z)$ direction appears associated to higher values, while for $q_x = q_y$ lines the peak structure becomes rather blured.

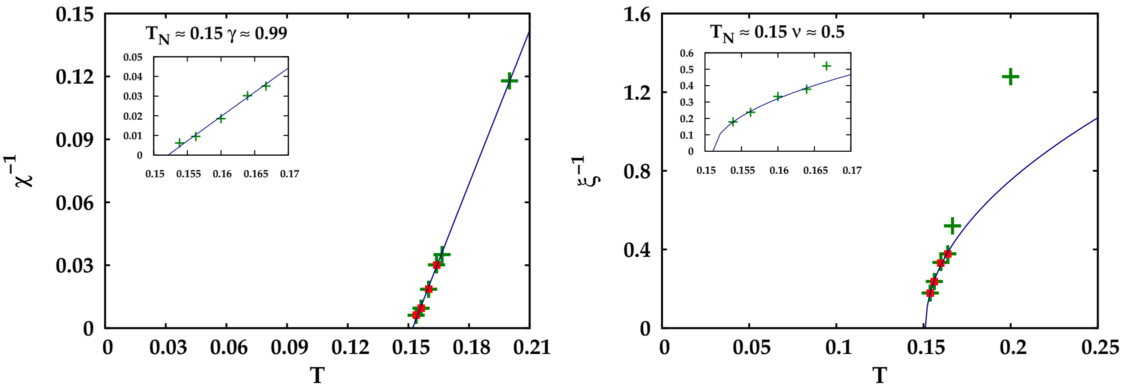

Figure 4.4: This figure shows the maximum values inverse susceptibility χ (left) and the inverse correlation length ξ (right), as a function of temperature, for n=0.850.

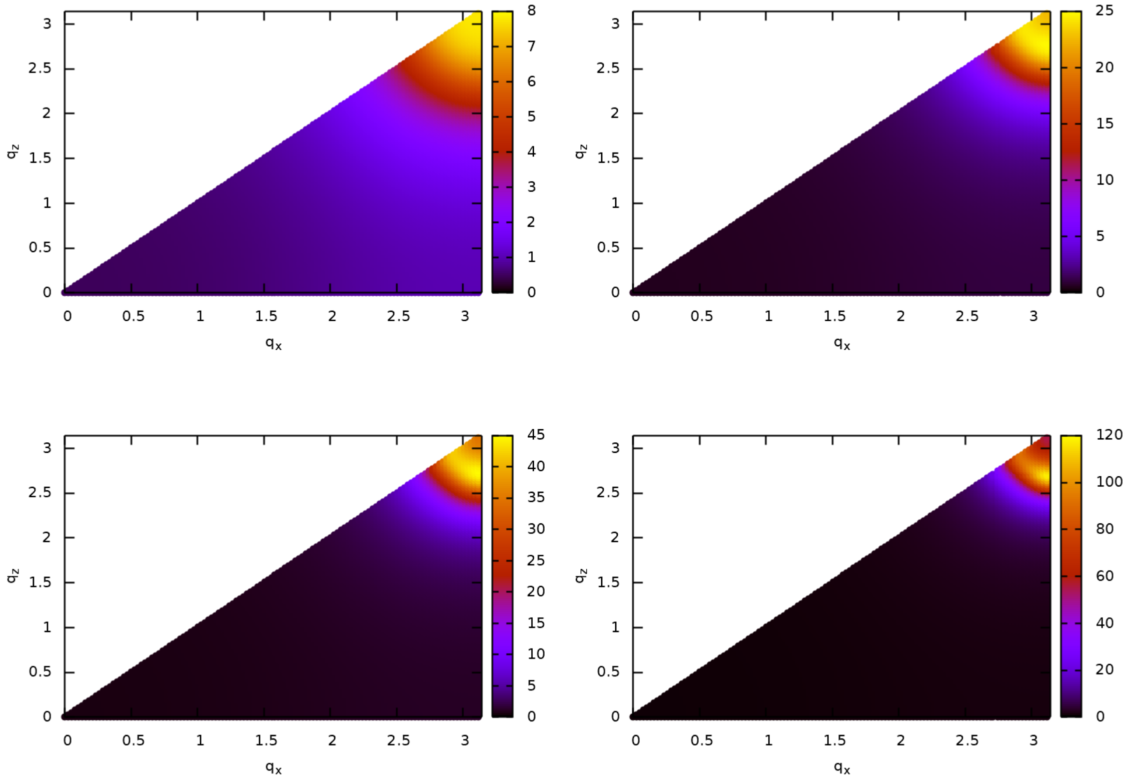

Figure 4.5: Momentum resolved susceptibility profile (q_x, π, q_z) for n=0.850, β=5 (left top), 6 (right top), 6.25 (left bottom), 6.50 (right bottom)

For the results at n=0.825, shown in Fig. 4.6, essentially the same argumentation holds as in the case of n=0.850. On the other hand, some changes should be outlined. While the susceptibility still show a conventional mean-field behavior, the inverse correlation length starts to display deviations from pure mean-field value $\nu \approx 0.5$ but now being $\nu \approx 0.6$. This circumstance might originates either from the numerical precision of the data or from the inapplicability of the standard Lorentzian Ornstein-Zernike relation between χ and ξ. In fact, it could be observed while performing the fitting procedure, that the region for a acceptable fit has been reduced from $[0, \pi]$ to a region $[Q - \delta, Q + \delta]$. Still the results do not deviate largely from mean-field values. In accordance with the results of n=0.850 an incommensurate behavior for the susceptibility (Fig. 4.7) can be observed. However, especially in case of low temperatures the $(\pi, \pi, \delta q_z)$ shaping is emerging more visibly.

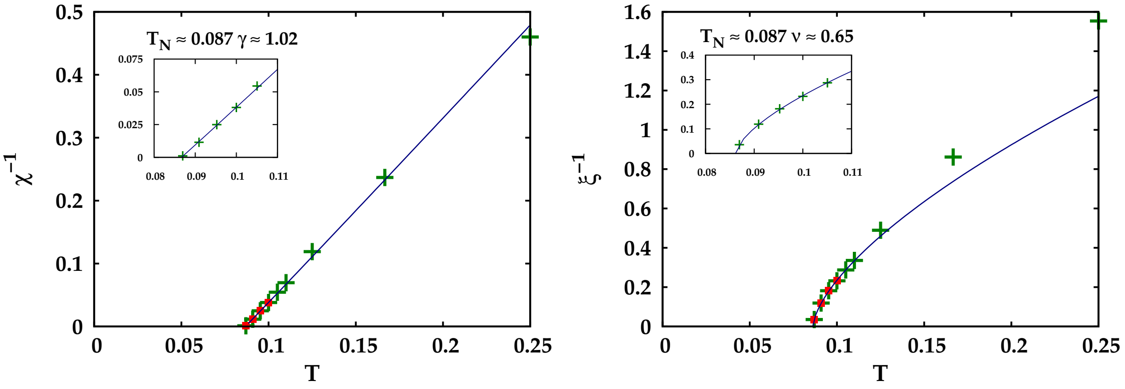

Figure 4.6: This figure shows the maximum values inverse susceptibility χ (left) and the inverse correlation length ξ (right), as a function of temperature, for n=0.825.

4.3 Quantum critical effects

Inside the quantum critical "funnel" n=0.8

At this doping level, intermediate temperature points might be already situated at the border or inside the quantum critical funnel schematically depicted: we find in Fig 3.2. Here both critical exponents γ and ν strongly deviate from their mean-field values $\gamma_q \approx 0.65$ and $\nu_q \approx 0.85$ with an almost complete inversion of the Fisher relation 3.13, shown in Fig. 4.8. The fit, however, also yields a finite ordering temperature, which might indicate that the points considered actually describe only a sharp crossover between an higher T (quantum critical?= and a lower $T \sim T_N$ (classical regime). In any case, for low-temperature points, we certainly leave the funnel-shaped are of quantum critical regime and both γ and

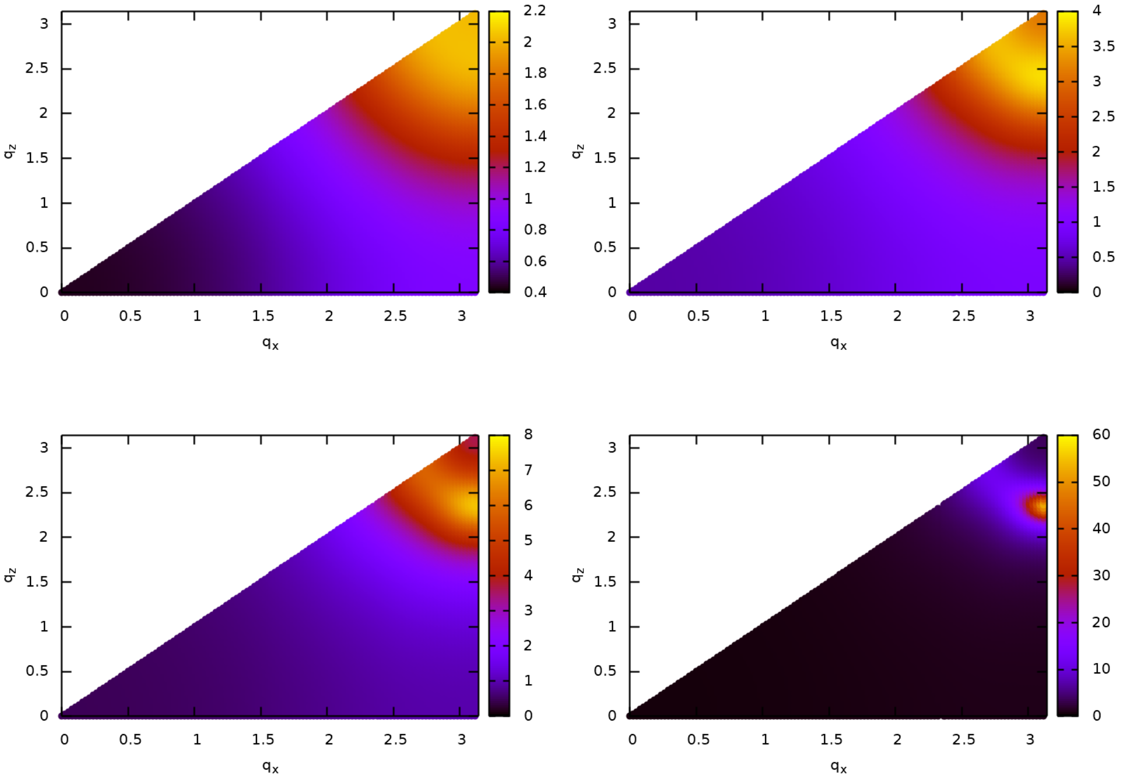

Figure 4.7: Momentum resolved susceptibility profile (q_x, π, q_z) for n=0.825, β=4 (left top), 6 (right top), 8 (left bottom), 11 (right bottom)

ν show again mean field behavior with $\gamma_c \approx 1$ and $\nu_c \approx 0.5$. At this doping the Néel-Temperature reaches $T_N \approx 0.0371$ indicating a QCP in proximity.

Beyond the QCP n=0.775

When overdoping the system at n=0.775 the situation, as shown in Fig. 4.9, appears as follows. For a intermediate temperature regime we obtain values for the critical exponents similar to the quantum critical ones, however, further investigation is needed to confirm this hypothesis. For the lowest temperature point ($T < 0.02$) we can observe a clear flattening of the data points and by extrapolating towards T=0 we get *a finite* value for the susceptibility, which can be interpreted as a conventional Fermi-liquid (or Pauli-like) behaviour.

It should be noted that the numerical treatment of these low-temperature points has become quite challenging, mostly because a higher number of Matsubara

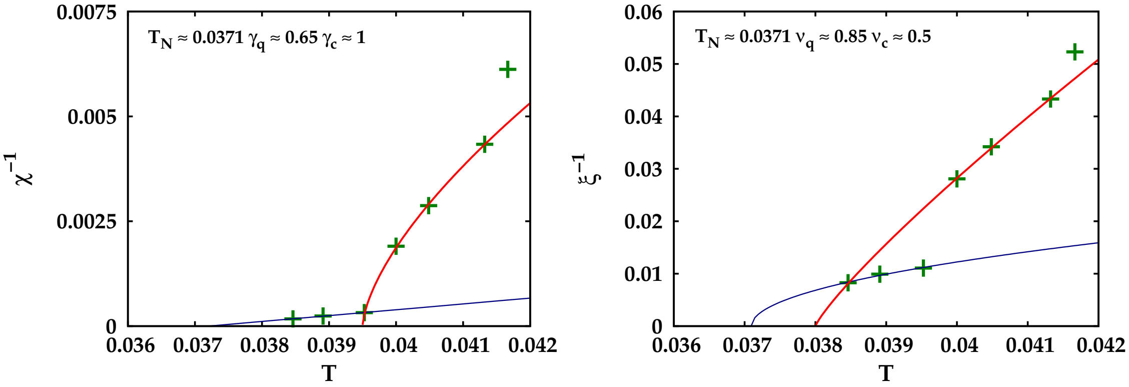

Figure 4.8: Maximum values inverse susceptibility χ (left) and the inverse correlation length ξ (right), as a function of temperature, for n=0.8. The blue show the fit for the classical critical region outside the quantum critical funnel γ_c, ν_c, while the red line fits point are situated inside the funnel γ_q, ν_q, or at its border if they describe a sharp crossover.

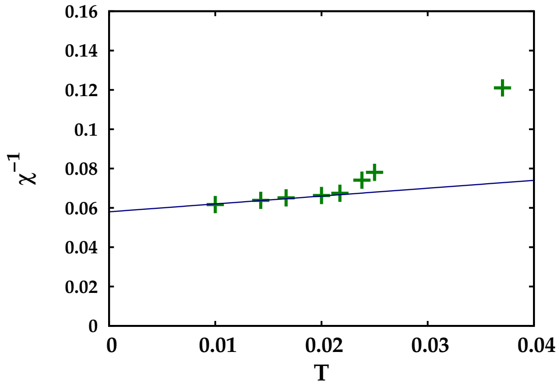

Figure 4.9: Maximum values inverse susceptibility χ as a function of temperature, for n=0.775.

frequencies is needed to perform correctly the calculations. This is the reason why data for the inverse correlation length needs a refined study and are not shown here.

Néel Temperature behaviour

Before coming to discuss the quantum critical point regime, we have a look at the Néel temperature as a function of doping, shown in Fig. 4.10. Comparing this picture with its DΓA counterpart in Fig. 3.10, observe as expected, systematically higher values for T_N. In fact, DMFT by neglecting all spatial fluctuations systematically overestimates phase transition temperatures with respect to DΓA. The suppression of T_N by increasing hole doping happens to be weaker (but only slightly) than for DΓA [3].

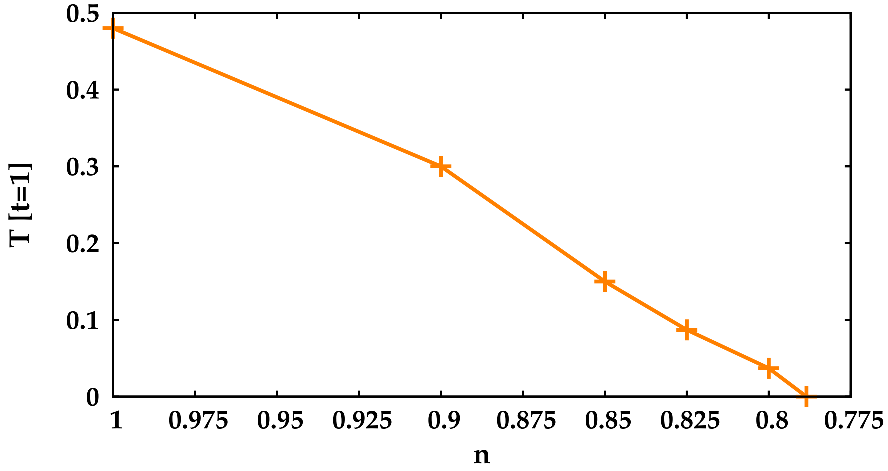

Figure 4.10: This figure shows the Néel temperature as a function of density n.

Non thermal critical exponents

As a preparatory step before discussing the critical behaviour at (or in immediate proximity) of the QCP we briefly discuss the functional behaviour of the non-thermal critical exponent for the susceptibility. Fig. 4.11 show the T=0 extrapolated finite values of χ^{-1} of "overdoped" phase diagram cuts (n=0.7875, 0.7825, 0.775). A linear function the form $a + bx$ is used for the fit of the three lowest-temperature points, as seen in Fig. 4.9. The fit is performed by least-squares method. With this method an estimate for the quantum critical point can be given, since the susceptibility scales with the following relation:

$$\chi^{-1}_{T=0} = (\delta - \delta_c)^{\gamma*} \tag{4.4}$$

with δ being the tunning parameter. The relation with n reads $\delta_c = 1 - n_c$.

This treatment is still preliminary (we have only 3 data point for n=0.7875 and n=0.7825), since in contrast to n=0.775 where data points show a convergent behaviour, especially for n=0.7875 (not explicitly shown here) the lowest-temperature point ($\beta = 100$) has been excluded from the fit as data it is not numerically precise for the determination of the critical exponent δ_c. In this case the number of Matsubara frequencies (here 150) is still not adequately chosen to correctly describe the behavior, which resulted in a significantly overestimated value for the inverse susceptibility. Therefore a 2P DMFT calculation (see Sec. 4.1) with 200 fermionic will have to be done. However, from the numerical point of view this will be extremely challenging. To overcome computational time limits on the *Vienna Scientific luster (VSC)*, the QMC sweep parameter will be reduced (from $5 \cdot 10^5$ to 10^5) and the number of nodes for the calculation will be set as high as possible (from currently 80 to 125, as this can increase the statistics of the calculation).

This fit might suggest a *linear* behaviour of the (non-thermal) quantum critical exponent yielding $n_c \approx 0.7884$. On the other hand for the inverse correlation length, due to numerical challenges at low temperatures, no estimate could made and thus further refined calculation with the previously describe adaption need to be performed to complete this new part of the work.

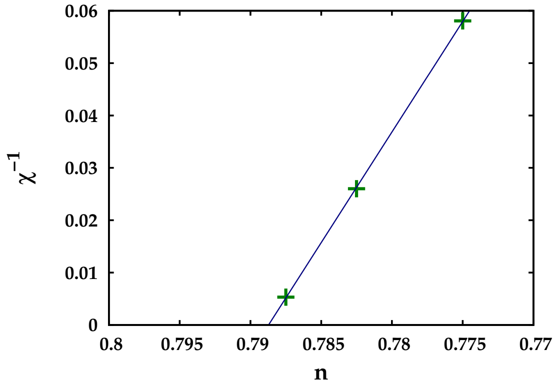

Figure 4.11: This figure shows the T=0 extrapolated values for the inverse susceptibility χ as a function of electron density.

4.4 Critical doping n=0.7885?

Finally we have arrived at a our estimated critical doping at n=0.7885. Here it can be seen from Fig. 4.12 that for low-temperature points again the frequency box of Matsubara frequencies is not large enough, resulting in progressively overestimated values for the inverse correlation length. This suspect becomes evidently when extrapolating the data for infinite frequencies. We can see in the right panel of Fig. 4.12, that we are still in a sort of“linear” frequency regime and the expected tendency to saturation towards a constant value has not been reached (in contrast to te assumed fitting function of Step 6 in 4.1). Here again calculations with a higher number of fermionic Matsubara frequencies need to be performed (at least 250 instead of 150). Also the same changes with respect to computational parameters, describe in the previous paragraphs need to be done to obtain reliable results. On the other hand, at the critical doping we might will observe a quantum critical behaviour for much higher temperature points (e.g., presumably in the interval between $\beta = 40$ to $\beta = 25$). Therefore we plan to perform future calculations in the enlarges T-interval, exploiting to our advantage te high-T impact of the underlying QCP.

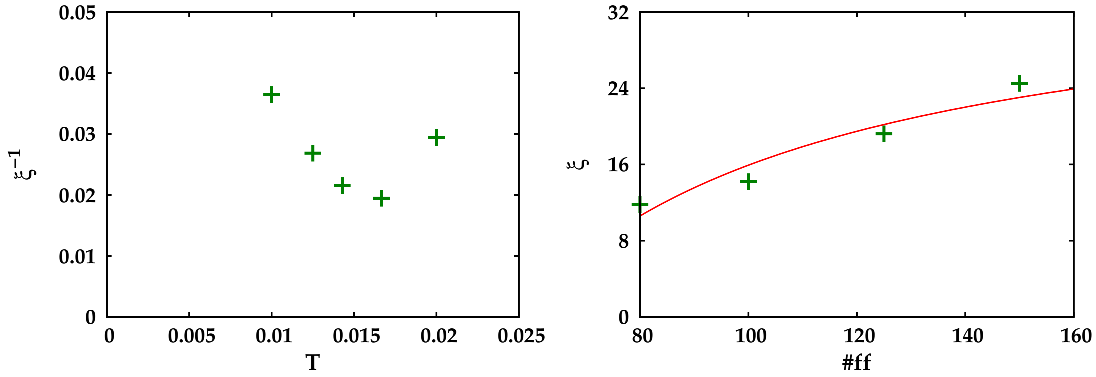

Figure 4.12: Maximum values inverse correlation length ξ (left), as a function of temperature, for n=0.7885. The right panel illustrates the values of the (not inverse) correlation for a different number of fermionic Matsubara frequencies ($\#ff$).

CHAPTER 5

Conclusion & Outlook

Physicists like to think that all you have to do is say, these are the conditions, now what happens next?

— Richard P. Feynman

In this thesis the hypothesis has been tested that DMFT treatment can be used to describe quantum critical behaviour of strongly correlated metal systems as in the prototype case of the 3D Hubbard model.

Our DMFT calculations have allowed to determine quite precisely the position of the magnetic QCP in the phase diagram of the 3D-Hubbard model as a function of hole-doping. Further, we have studied the critical properties of te systems in both sides of the QCP. In particular, it could be shown that leaving the classical critical parameter regime, where the critical exponents appeared mean-field like $\gamma \approx 1$ and $\nu \approx 0.5$, when entering the quantum critical funnel-shaped phase diagram region for both investigated critical exponents γ and ν, abrupt changes could be observed. In case of n=0.8 the values inside the funnel changed to $\gamma \approx 0.65$ and $\nu \approx 0.85$, which display a promising trend with respect to previous DΓA studies [3]. This results are driven by Fermi surface features, in this case Kohn lines or Kohn points. As DMFT preserves the information about the FS geometry and correctly captures temporal fluctuations, crucial for the description of quantum criticality, this behaviour has been initially expected.

However at the presumed critical doping at n=0.7885 low temperature point could not be obtained by enough numerical precision, as shown in Fig. 5.2. Therefore

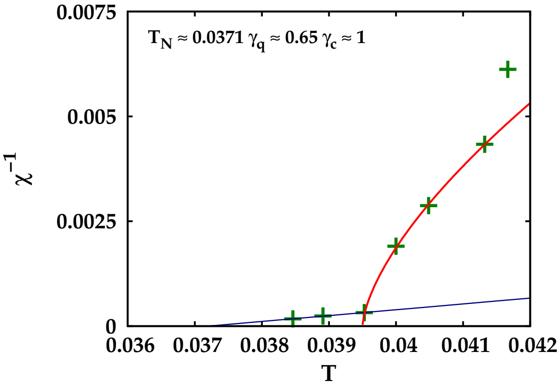

Figure 5.1: This figure shows the quantum critical behaviour the critical exponent γ_q at n=0.8

future calculations with higher frequency boxes will need to be performed. The same presumably incorrect low-temperature behaviour could also be observed for slightly overdoped phase diagram "cuts". Here again numerical precision will have to be increased.

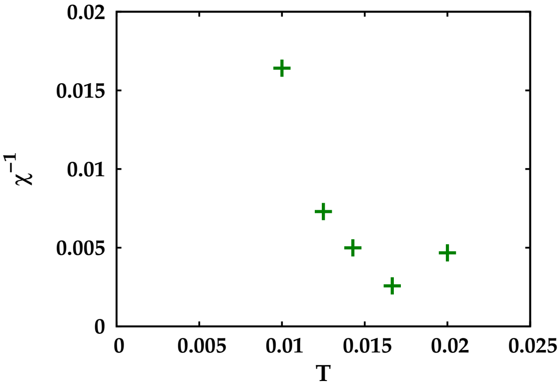

Figure 5.2: This figure illustrates the fact of using a not sufficient number of fermionic Matsubara frequencies resulting in an overestimate for the inverse susceptibility.

In case of the critical doping, however, quantum critical features should manifest at a broader temperature range including intermediate values ($\beta = 40$ to $\beta = 25$ parameter regime). Thus future calculation in this, from the numerical point of view more precisely accessible, phase diagram region will be performed.

Moreover, although the main focus in this work has been on thermal critical exponents, as mentioned in the last part of Sec. 4.3, also non thermal critical exponents are of great interest since they complete they characterization of a quantum phase transition and they represent a helpful *tool* for identifying more precisely, the position of a quantum critical point. Due to the numerical challenges during the extrapolation of the required low temperature data points for functional fits, further investigation will be needed to prove whether this exponents show a behaviour as predicted by HMM theory, which would pave the route for interesting new investigations on the quantum criticality in correlated systems.

The promising results of this work show a concrete possibility that the deviations from te HMM prediction can be already captured for correlated metallic systems at the level of DMFT, without the need of more complex DΓA calculations. IT definitely confirmed this information can be of crucial importance for the realistic treatment f quantum criticality in correlated materials.

List of Figures

1.1 This figure, taken from [1], schematically shows the phase transition temperature T_c (light-blue) as a function of a non-thermal parameter g. At a critical value g_c, which defines the QCP, the transition is completely suppressed and $T_c = 0$. 2

2.1 The illustration is taken from [4] and shows the two possibilities for the electrons in a “fishy” way: either adding (top picture) or removing (bottom picture) an electron at $\vec{x}', t'$ and letting the electron or respectively the hole propagate until $\vec{x}, t$, where it is removed (or added) again . . . 7
2.2 When expanding the interacting Green function in the Dyson equation a resulting infinite sum of 1P reducible diagrams appears. These corresponding classification can be done by an imaginary pair of scissors showing that through cutting an internal Green function line two separate Feynman diagrams can be obtained [7]. 10
2.3 The illustration taken from [15] shows the electronic microscopic processes of the Hubbard model: Hopping from site i to j and ii whenever two electrons with opposite spin are on the same lattice site, the local Coulomb interaction U must be paid. 13
2.4 This illustration shows Self Energy expressed as the sum of all one particle irreducible diagrams. 16
2.5 This figure, which is taken from [15], illustrates that DMFT is essentially a mapping of the d-Dimensional Hubbard Model and its corresponding self-energy $\Sigma(k, \omega)$ onto a single site (described by its determined, auxiliary AIM). Thus the impurity and the bath electrons hybridize resulting in a local problem, where the self-energy is momentum independent. . . 17
2.6 This figure [22] summarizes the process for performing a DMFT self consistency loop. As highlighted in the picture the most challenging step is the numerical solution of the AIM. 18
2.7 This figure, which has been taken from [31] show a particle-hole scattering event on the left side and a particle-particle one on the right 22

2.8 This figure, which has been again taken from [31] shows the diagram corresponding to the independent propagation of two particles as well as that describing the scattering events. The sum of the two contributions yields the generalized susceptibility $\chi_{\sigma,\sigma'}^{\nu,\nu',\omega}$ 23

2.9 Here one can see the diagrammtic decompostion of the Full Vertex F into a fully irreducible part Λ and reducible parts Φ_r for the specific channels $r = (pp, ph, \overline{ph})$ [31] 24

2.10 Ladder decomposition of the response function $\chi(q, i\omega)$. 28

3.1 This adapted figure from [34] depicts the classical critical regime of a 2^{nd} order phase transition. 31

3.2 This figure from [34] depicts the phase diagram region of quantum critical behaviour, where temporal fluctuations are dominant. 33

3.3 This figure from [36] shows the "high temperature" properties of a QCP, which perfectly matches the schematization of Fig. 3.1. 35

3.4 The dotted line show the functional behaviour of the free energy per Volume f for $T > T_c$, the continuous one for $T = T_c$ and the dashed one for $T < T_c$ 37

3.5 This picture (taken from [40]) shows the Néel Temperature of the 3D Hubbard Model as a function of the interaction strength U (in unit of $2\sqrt{6}t = 1$) for DMFT and its diagrammatic extensions as well as (for comparison) the ones of the Heisenberg model. 40

3.6 This picture (taken from [39]) shows the inverse susceptibility for different values of U. In the lower inset a linear mean field (DMFT) behaviour is shown, while in the upper one the deviation between DΓA and DMFT behaviour is zoomed in for U=1.25 and U=1.50. 41

3.7 This figure taken from [46], show the comparison between two numerical fits for the inverse particle-particle susceptibility. The red-dashed line, which takes sub-to-leading order into account show a slightly lower critical temperature. The latter seems in better agreement with the remarkably different critical exponents 42

3.8 This figure, adapted from [3], shows the Néel-Temperature as a function of the doping concentration. For a critical density $n = n_c \approx 0.8$. The Néel temperature vanishes, marking the existence of a quantum critical point. 44

3.9 In this picture, taken from [51], Kohn lines in the 3D Fermi surface of the simple cubic lattice, with assumed nearest-neighbor hopping (left) are shown. In the right panel a 2D cut of the left picture including the SDW vector $\vec{Q}_0$ can be seen. 45

3.10 This figure which has been taken from [51] show the inverse correlation length ξ^{-1} in the upper row as well as the inverse susceptibility χ^{-1} for n=1.0 and n=0.87. For the fitted functions the green points have been considered. 45
3.11 This figure which has been taken from [51] show the inverse correlation length ξ^{-1} in the upper row as well as the inverse susceptibility χ^{-1} for n=0.805 and n=0.79. For the fitted functions the green points have been considered. 46

4.1 This figure illustrates the fit for the correlation length frequency extrapolation for n=0.825 and $\beta = 10$. The x-axis show the number of fermionic frequencies used for the calculations of Step 3. 49
4.2 This figure shows the maximum values inverse susceptibility χ (left) and the inverse correlation length ξ (right), as a function of temperature, for n=1.0. The fitted blue lines have been used for obtaining numerical values of the critical exponents γ and ν. Only low-temperature points have been used for the fit (red dots as well as insets). This procedure has been repeated for all dopings. 50
4.3 This figure shows the maximum values inverse susceptibility χ (left) and the inverse correlation length ξ (right), as a function of temperature, for n=0.9. 51
4.4 This figure shows the maximum values inverse susceptibility χ (left) and the inverse correlation length ξ (right), as a function of temperature, for n=0.850. 52
4.5 Momentum resolved susceptibility profile (q_x, π, q_z) for n=0.850, β=5 (left top), 6 (right top), 6.25 (left bottom), 6.50 (right bottom) 52
4.6 This figure shows the maximum values inverse susceptibility χ (left) and the inverse correlation length ξ (right), as a function of temperature, for n=0.825. 53
4.7 Momentum resolved susceptibility profile (q_x, π, q_z) for n=0.825, β=4 (left top), 6 (right top), 8 (left bottom), 11 (right bottom) 54
4.8 Maximum values inverse susceptibility χ (left) and the inverse correlation length ξ (right), as a function of temperature, for n=0.8. The blue show the fit for the classical critical region outside the quantum critical funnel γ_c, ν_c, while the red line fits point are situated inside the funnel γ_q, ν_q, or at its border if they describe a sharp crossover. 55
4.9 Maximum values inverse susceptibility χ as a function of temperature, for n=0.775. 55
4.10 This figure shows the Néel temperature as a function of density n. . . . 56
4.11 This figure shows the T=0 extrapolated values for the inverse susceptibility χ as a function of electron density. 57

4.12 Maximum values inverse correlation length ξ (left), as a function of temperature, for n=0.7885. The right panel illustrates the values of the (not inverse) correlation for a different number of fermionic Matsubara frequencies ($\#ff$). 58

5.1 This figure shows the quantum critical behaviour the critical exponent γ_q at n=0.8 60

5.2 This figure illustrates the fact of using a not sufficient number of fermionic Matsubara frequencies resulting in an overestimate for the inverse susceptibility. 60

Bibliography

[1] I. Frérot and T. Roscilde. Reconstructing the quantum critical fan of strongly correlated systems using quantum correlations. *Nature communications*, **10**, 577 (2019).

[2] H. v Löhneysen, A. Rosch, M. Vojta, and P. Wölfle. Fermi-liquid instabilities at magnetic quantum phase transitions. *Rev. Mod. Phys.*, **79**, 1015 (2007).

[3] T. Schäfer. *Classical and quantum phase transitions in strongly correlated electron systems.* PhD thesis, Technische Universität Wien, (2016).

[4] A. Zagoskin. *Quantum Theory of Many-Body Systems: Techniques and Applications.* Springer Publishing Company, Incorporated, 2^{nd} edition, (2014).

[5] G. C. Wick. Properties of bethe-salpeter wave functions. *Phys. Rev.*, **96**, 1124 (1954).

[6] A. Toschi. Quantum field theory for many-electron systems: The feynman diagrammatic formalism. *Bandstructure meets quantum field theory - Cecam Workshop*, (2018).

[7] Autumn School on Correlated Electrons, Jülich. *DMFT at 25: Infinite Dimensions*, volume 8 of *Modeling and Simulation.* Forschungszentrum Jülich Zentralbibliothek, Verlag, (2018).

[8] A. Damascelli, Z. Hussain, and Z.-X. Shen. Angle-resolved photoemission studies of the cuprate superconductors. *Rev. Mod. Phys.*, **75**, 473 (2003).

[9] J. Hubbard. Electron correlations in narrow energy bands. *Proceedings of the Royal Society of London. Series A, Mathematical and Physical Sciences*, **276**, (1963).

[10] M. C. Gutzwiller. Effect of correlation on the ferromagnetism of transition metals. *Phys. Rev. Lett.*, **10**, 159 (1963).

[11] J. Kanamori. Electron Correlation and Ferromagnetism of Transition Metals. *Progress of Theoretical Physics*, **30**, 275 (1963).

[12] A. Altland and B. Simons. *Condensed Matter Field Theory.* Cambridge University Press, (2010).

[13] A. Georges, G. Kotliar, W. Krauth, and M. J. Rozenberg. Dynamical mean-field theory of strongly correlated fermion systems and the limit of infinite dimensions. *Rev. Mod. Phys.*, **68**, 13 (1996).

[14] A. Toschi, A. A. Katanin, and K. Held. Dynamical vertex approximation: A step beyond dynamical mean-field theory. *Phys. Rev. B*, **75**, 045118 (2007).

[15] D. Vollhardt. Dynamical mean-field theory of electronic correlations in models and materials. *AIP Conference Proceedings*, **1297**, (2010).

[16] J. de Boer W.J. de Haas and G.J. van dën Berg. The electrical resistance of gold, copper and lead at low temperatures. *Physica*, **1**, 1115 (1934).

[17] J. Kondo. Resistance Minimum in Dilute Magnetic Alloys. *Progress of Theoretical Physics*, **32**, 37 (1964).

[18] P. W. Anderson. Localized magnetic states in metals. *Phys. Rev.*, **124**, 41 (1961).

[19] D. Vollhardt. Dynamical mean-field theory for correlated electrons. *Bandstructure meets quantum field theory - Cecam Workshop*, (2018).

[20] R. J. Baxter. *Exactly Solved Models in Statistical Mechanics.* Academic Press, London, (1982).

[21] W. Metzner and D. Vollhardt. Correlated lattice fermions in $d = \infty$ dimensions. *Phys. Rev. Lett.*, **62**, 324 (1989).

[22] A. Toschi. *Strong Electronic Correlation in Dynamical Mean Field Theory and beyond.* Technische Universität Wien, (2011).

[23] J. E. Hirsch and R. M. Fye. Monte carlo method for magnetic impurities in metals. *Phys. Rev. Lett.*, **56**, 2521 1986.

[24] E. Gull, A. J. Millis, A. Lichtenstein, A. Rubtsov, M. Troyer, and P. Werner. Continuous-time monte carlo methods for quantum impurity models. *Rev. Mod. Phys.*, **83**, 349 (2011).

[25] A. Rubtsov and A. Lichtenstein. Continuous-time quantum monte carlo method for fermions: Beyond auxiliary field framework. *Journal of Experimental and Theoretical Physics Letters*, **80**, 61 (2004).

[26] P. Werner, A. Comanac, L. De'Medici, M. Troyer, and A. Millis. Continuous-time solver for quantum impurity models. *Phys. Rev. Lett.*, 076405 (2006).

[27] N. Parragh, M. Wallerberger, A. Hausoel, P. Gunacker, and G. Sangiovanni. *w2dynamics* - strong coupling impurity solver. `http://www.ifp.tuwien.ac.at/forschung/arbeitsgruppen/cms/softwaredownload/w2dynamics/`.

[28] E. Gull, P. Werner, A. Millis, and M. Troyer. Performance analysis of continuous-time solvers for quantum impurity models. *Phys. Rev. B*, **76**, 235123 (2007).

[29] A. Georges and W. Krauth. Physical properties of the half-filled hubbard model in infinite dimensions. *Phys. Rev. B*, **48**, 7167 (1993).

[30] Autumn School on Correlated Electrons, Jülich. *DMFT at 25: Infinite Dimensions*, volume 4 of *Modeling and Simulation*. Forschungszentrum Jülich Zentralbibliothek, Verlag, (2014).

[31] G. Rohringer, A. Valli, and A. Toschi. Local electronic correlation at the two-particle level. *Phys. Rev. B*, **86**, 125114 (2012).

[32] C. Di Castro and R. Raimondi. *Statistical Mechanics and Applications in Condensed Matter*. Cambridge University Press, (2015).

[33] P. Mohn. *Magnetism in the solid state: an introduction*. Springer Science & Business Media, (2006).

[34] Quantumphasetransition. `https://de.wikipedia.org/wiki/Datei:QuantumPhaseTransition.png`. Accessed: 05.05.2019.

[35] Edward Armand Guggenheim. *Thermodynamics-an advanced treatment for chemists and physicists*. North-Holland Publishing Company, (1985).

[36] J. Custers, P. Gegenwart, H. Wilhelm, K. Neumaier, Y. Tokiwa, O. Trovarelli, C. Geibel, F. Steglich, C. Pépin, and P. Coleman. The break-up of heavy electrons at a quantum critical point. *Nature*, **424**, 524 (2003).

[37] J. Hertz. Quantum critical phenomena. *Phys. Rev. B*, **14**, 1165 (1976).

[38] J. Rech. *Macroscopic quantum phenomena in strongly interacting fermionic systems*. PhD thesis, Université Paris, (2006).

[39] G. Rohringer, A. Toschi, A. Katanin, and K. Held. Critical properties of the half-filled hubbard model in three dimensions. *Phys. Rev. Lett.*, **107**, 256402 (2011).

[40] G. Rohringer and A. Toschi. Impact of nonlocal correlations over different energy scales: A dynamical vertex approximation study. *Phys. Rev. B*, **94**, 125144 (2016).

[41] K. Held, G. Keller, V. Eyert, D. Vollhardt, and V. Anisimov. Mott-hubbard metal-insulator transition in paramagnetic V_2O_3: An LDA+DMFT (QMC) study. *Phys. Rev. Lett.*, **86**, 5345 (2001).

[42] A. Toschi, P. Barone, M. Capone, and C. Castellani. Pairing and superconductivity from weak to strong coupling in the attractive hubbard model. *New Journal of Physics*, **7**, 7 (2005).

[43] A. Toschi, M. Capone, M. Ortolani, .P Calvani, S. Lupi, and C. Castellani. Temperature dependence of the optical spectral weight in the cuprates: role of electron correlations. *Phys. Rev. Lett.*, **95**, 097002 (2005).

[44] D. Hirschmeier, H. Hafermann, E. Gull, A. Lichtenstein, and A.E. Antipov. Mechanisms of finite-temperature magnetism in the three-dimensional hubbard model. *Phy. Rev. B*, **92**, 144409 (2015).

[45] G. Rohringer, H. Hafermann, A. Toschi, A. A. Katanin, A. E. Antipov, M. I. Katsnelson, A. I. Lichtenstein, A. N. Rubtsov, and K. Held. Diagrammatic routes to nonlocal correlations beyond dynamical mean field theory. *Rev. Mod. Phys.*, **90**, 25003 (2018).

[46] L. Del Re, M. Capone, and A. Toschi. Dynamical vertex approximation for the attractive hubbard model. *Phys. Rev. B*, **99**, 45137 (2019).

[47] P. Sémon and A. Tremblay. Importance of subleading corrections for the mott critical point. *Phys. Rev. B*, **85**, 201101 (2012).

[48] A. Katanin, A. Toschi, and K. Held. Comparing pertinent effects of antiferromagnetic fluctuations in the two-and three-dimensional hubbard model. *Phys. Rev. B*, **80**, 075104 (2009).

[49] Y. Vilk and A. Tremblay. Non-perturbative many-body approach to the hubbard model and single-particle pseudogap. *Journal de Physique I*, **7**, 1309 (1997).

[50] A. Daré and G. Albinet. Magnetic properties of the three-dimensional hubbard model at half filling. *Phys. Rev. B*, **61**, 4567 (2000).

[51] T. Schäfer, A. A. Katanin, K. Held, and A. Toschi. Interplay of correlations and kohn anomalies in three dimensions: Quantum criticality with a twist. *Phys. Rev. Lett.*, **119**, 46402 (2017).